Supplementary Information

Rational design of metal–organic cages to increase the number of components via dihedral angle control

Tsukasa Abe,[1] Keisuke Takeuchi,[1] Masahiro Higashi,[2] Hirofumi Sato,[3,4] and Shuichi Hiraoka[1]*

[1]Department of Basic Science, Graduate School of Arts and Sciences, The University of Tokyo, Tokyo 153-8902, Japan

[2]Department of Complex Systems Science, Graduate School of Informatics, Nagoya University, Nagoya 464-8601, Japan

[3]Department of Molecular Engineering, Kyoto University, Kyoto 615-8510, Japan

[4]Fukui Institute for Fundamental Chemistry, Kyoto University, Kyoto 606-8103, Japan

*Correspondence: hiraoka-s@g.ecc.u-tokyo.ac.jp

Contents

Supplementary Methods

Synthesis of 3

In a 100-mL sealed tube flask, 1,3,5-tribromo-2,4,6-trimethylbenzene (357 mg, 1.0 mmol, 1 eq.), 4-pyridylboronic acid (1.23 g, 10 mmol, 10 eq.), K_3PO_4 (2.55 g, 12 mmol, 12 eq.), $Pd_2(dba)_3$ (20.1 mg, 22 μmol, 0.022 eq.), and SPhos (18.1 mg, 44 μmol, 0.044 eq.) were mixed under inert atmosphere in *n*-butanol (40 mL). The resulting mixture was stirred at 80 °C for 3 days. After cooling to room temperature, the reaction mixture was filtered, and the filtrate was evaporated to remove the solvent. The residue was added to H_2O (10 mL), and extraction was performed using $CHCl_3$ (20 mL, three times). The organic layer was dried over anhydrous $MgSO_4$, and the solvent was removed by evaporation to yield a yellow solid. After purification by silica gel column chromatography (Eluent: AcOEt/*n*-Hexane = 3:1), tritopic ligand 3 was obtained as a colorless solid (42 mg, 0.15 mmol, 15 %). ^{1}H NMR (500 MHz, CD_2Cl_2, 298 K): δ 8.63 (dd, *J* = 2.0 and 4.3 Hz, 4 H), 7.11 (dd, *J* = 2.0 and 4.3 Hz, 4 H), 7.07 (s, 1 H), 2.01 (s, 6 H), 1.54 (s, 3 H). ^{13}C NMR (125 MHz, CD_2Cl_2, 298 K): δ 150.4, 149.7, 137.6, 135.2, 132.6, 129.4, 125.0, 20.7, 18.9.

HRMS (ESI-TOF) *m/z*: [**3**+H]$^+$ Calcd for $C_{19}H_{19}N_2$ 275.1543, Found 275.1542.

Supplementary Figures

Crystal structure of the $[Pd_{12}2_8]^{24+}$ open icosahedron

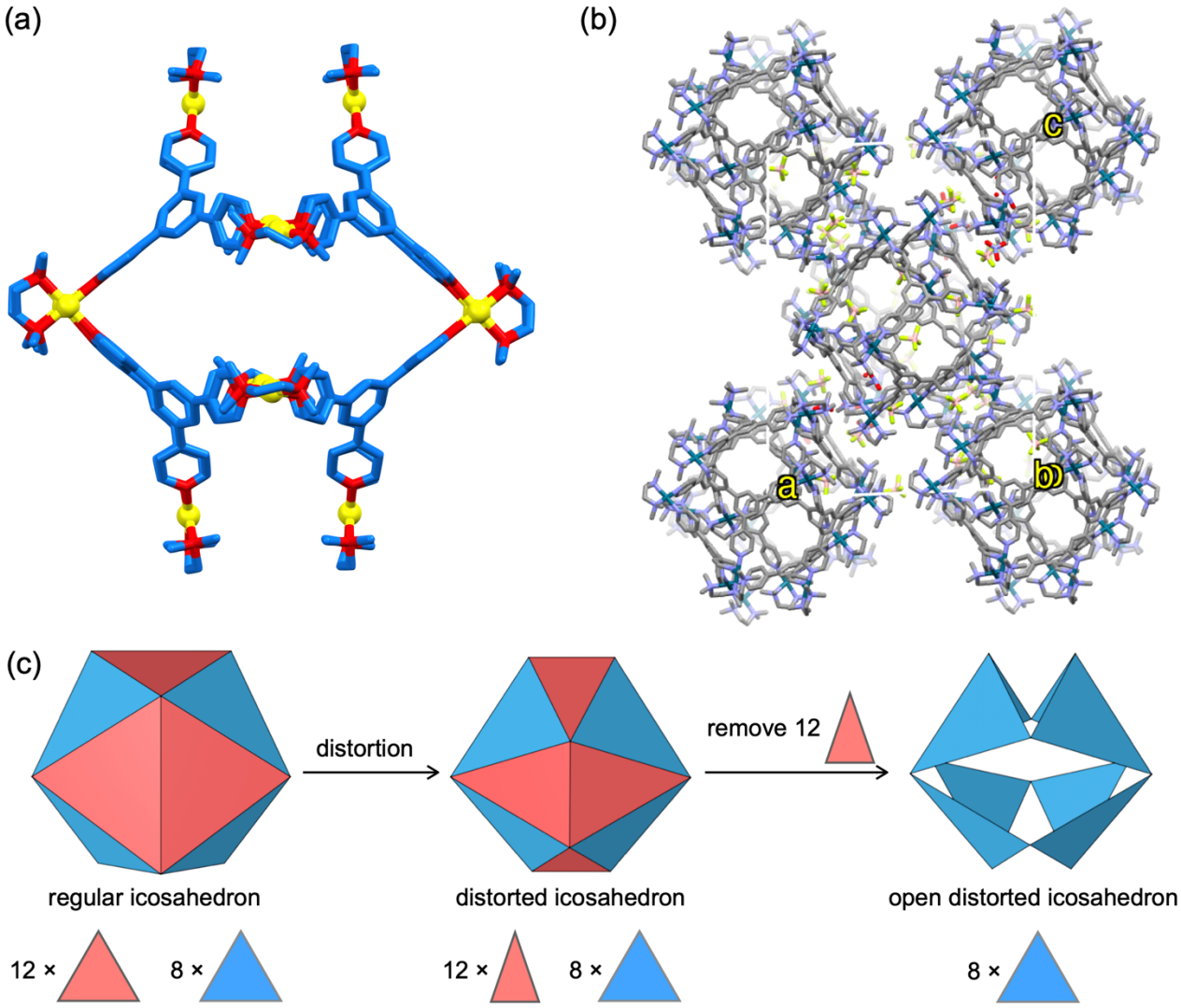

Supplementary Fig. 1. The crystal structure of the $[\boldsymbol{Pd}_{12}\boldsymbol{2}_8]^{24+}$ open icosahedron. Color labels: Yellow = Pd; Blue = C; Red = N. (a) A view from the M_4L_4 window. (b) A view of the packing structure of $[\boldsymbol{Pd}_{12}\boldsymbol{2}_8]^{24+}$ from *b*-axis. Color labels: Peacock green = Pd; Gray = C; Purple = N; Red = O; Baby pink = B; light lime green = F. (c) Schematic representation of $[\boldsymbol{Pd}_{12}\boldsymbol{2}_8]^{24+}$. The original structure of $[\boldsymbol{Pd}_{12}\boldsymbol{2}_8]^{24+}$ is a distorted icosahedron, in which twelve faces in red are isosceles triangles, and eight faces in blue are regular triangles. The structure of $[\boldsymbol{Pd}_{12}\boldsymbol{2}_8]^{24+}$ is generated by removing twelve isosceles triangles in red. 12 *cis*-protected Pd(II) ions ($\boldsymbol{Pd}^{2+}$) on the apexes are omitted.

Dynamic motion in the $[Pd_{12}2_8]^{24+}$ open icosahedron

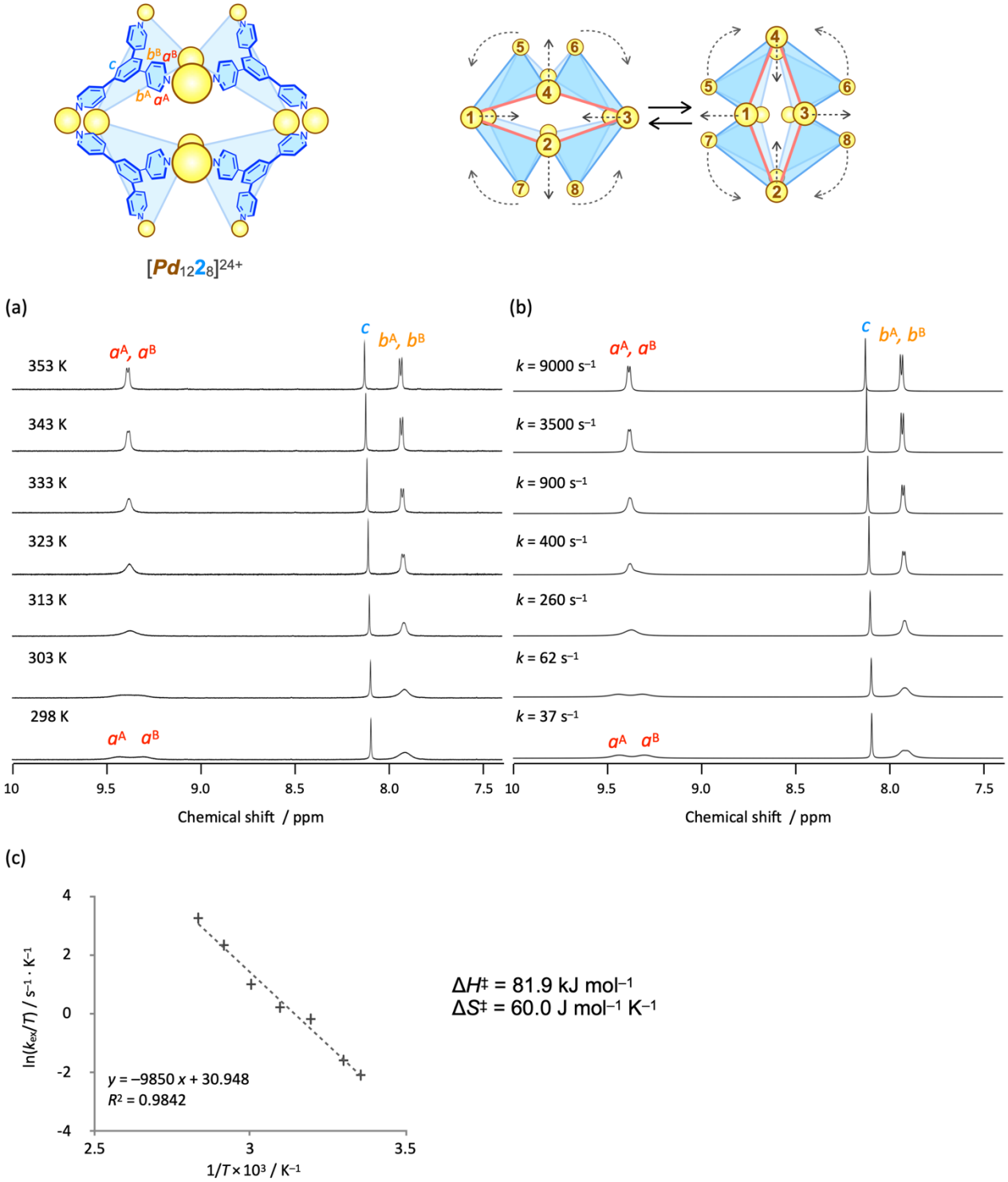

Supplementary Fig. 2. (a) Variable-temperature ^{1}H NMR spectra of the $[Pd_{12}2_8]^{24+}$ open icosahedron (500 MHz, CD_3NO_2). (b) Simulated ^{1}H NMR spectra with rate constants. (c) The Eyring plot to obtain kinetic parameters for the dynamic motion in $[Pd_{12}2_8]^{24+}$.

Characterization of the $[Pd_{12}\mathbf{2}_8]^{24+}$ open icosahedron in solution

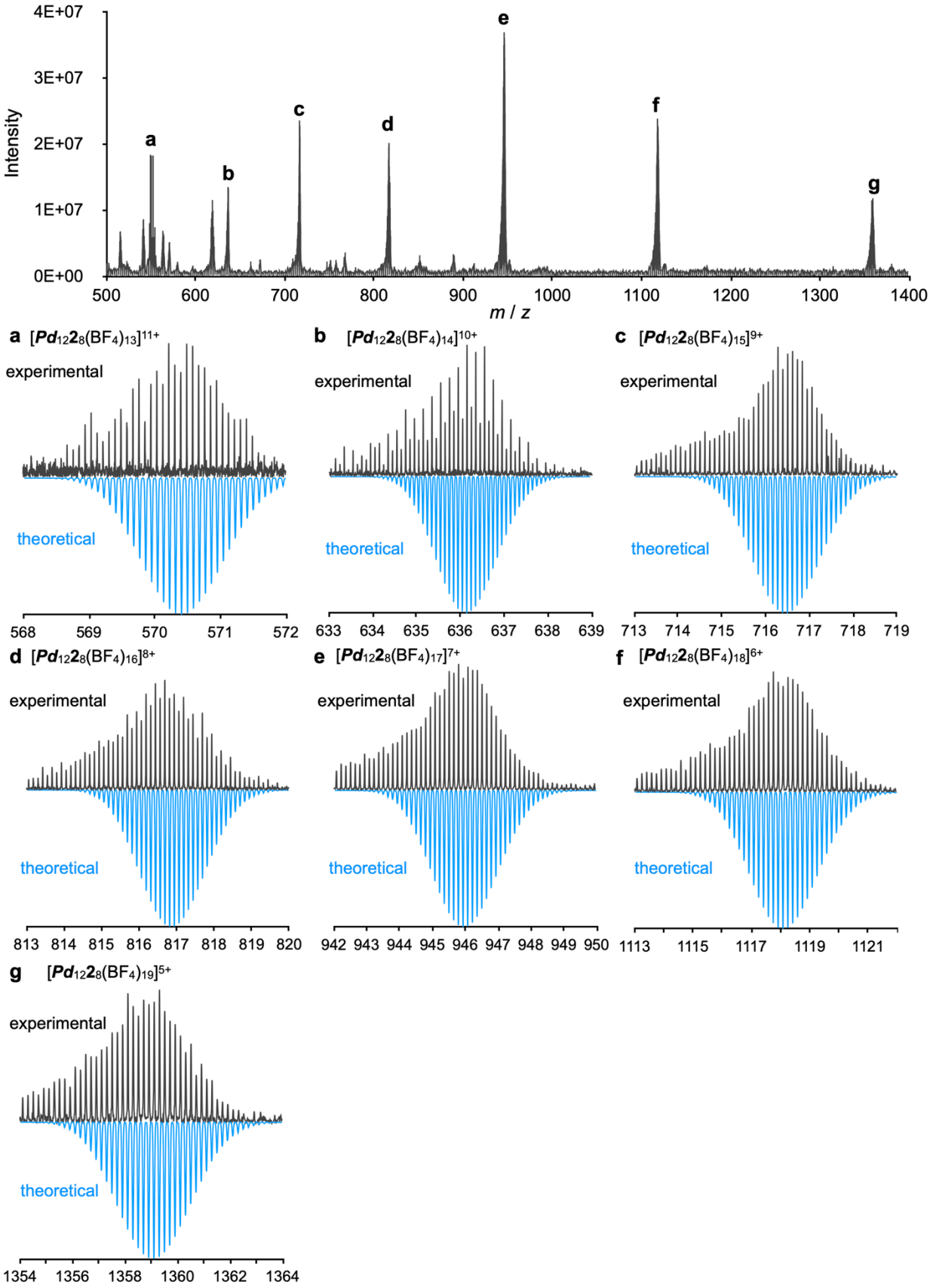

Supplementary Fig. 3. CSI FT-ICR MS spectrum of the $[Pd_{12}\mathbf{2}_8]^{24+}$ open icosahedron from $[Pd(CH_3CN)_2](BF_4)_2$ and **2** in the presence of *n*-$Bu_4N{\cdot}NO_3$ in CH_3NO_2, diluted with H_2O. (a) $[Pd_{12}\mathbf{2}_8(BF_4)_{13}]^{11+}$, (b) $[Pd_{12}\mathbf{2}_8(BF_4)_{14}]^{10+}$, (c) $[Pd_{12}\mathbf{2}_8(BF_4)_{15}]^{9+}$, (d) $[Pd_{12}\mathbf{2}_8(BF_4)_{16}]^{8+}$, (e) $[Pd_{12}\mathbf{2}_8(BF_4)_{17}]^{7+}$, (f) $[Pd_{12}\mathbf{2}_8(BF_4)_{18}]^{6+}$, and (g) $[Pd_{12}\mathbf{2}_8(BF_4)_{19}]^{5+}$.

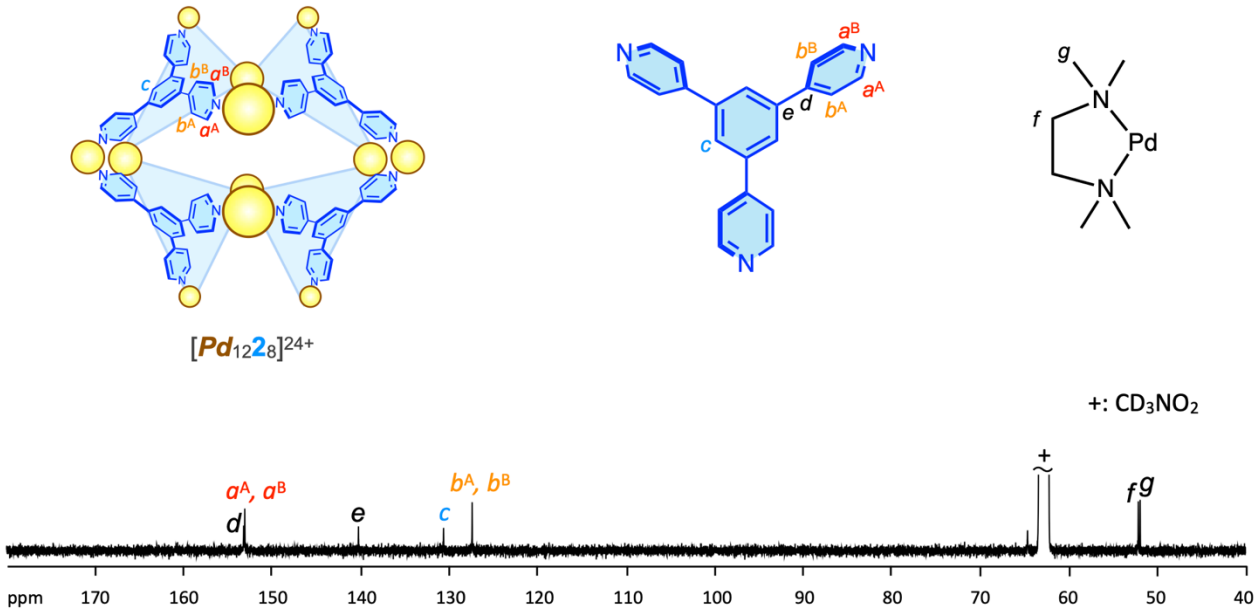

Supplementary Fig. 4. ^{13}C NMR spectrum of the [***Pd***$_{12}$**2**$_8$]$^{24+}$ open icosahedron (125 MHz, CD_3NO_2, 298 K).

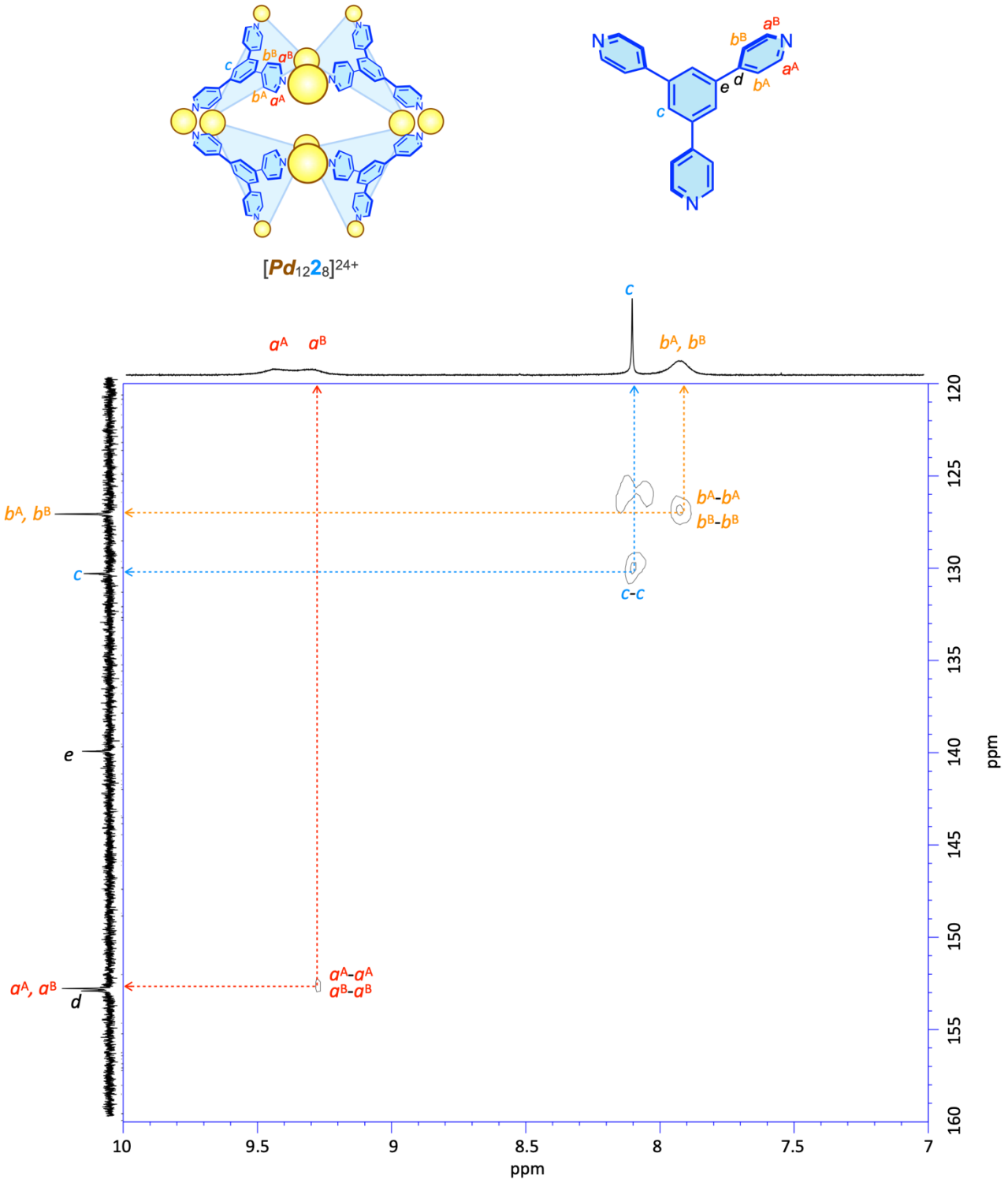

Supplementary Fig. 5. HMQC spectrum of the $[\boldsymbol{Pd}_{12}\mathbf{2}_8]^{24+}$ open icosahedron (500 MHz, CD_3NO_2, 298 K).

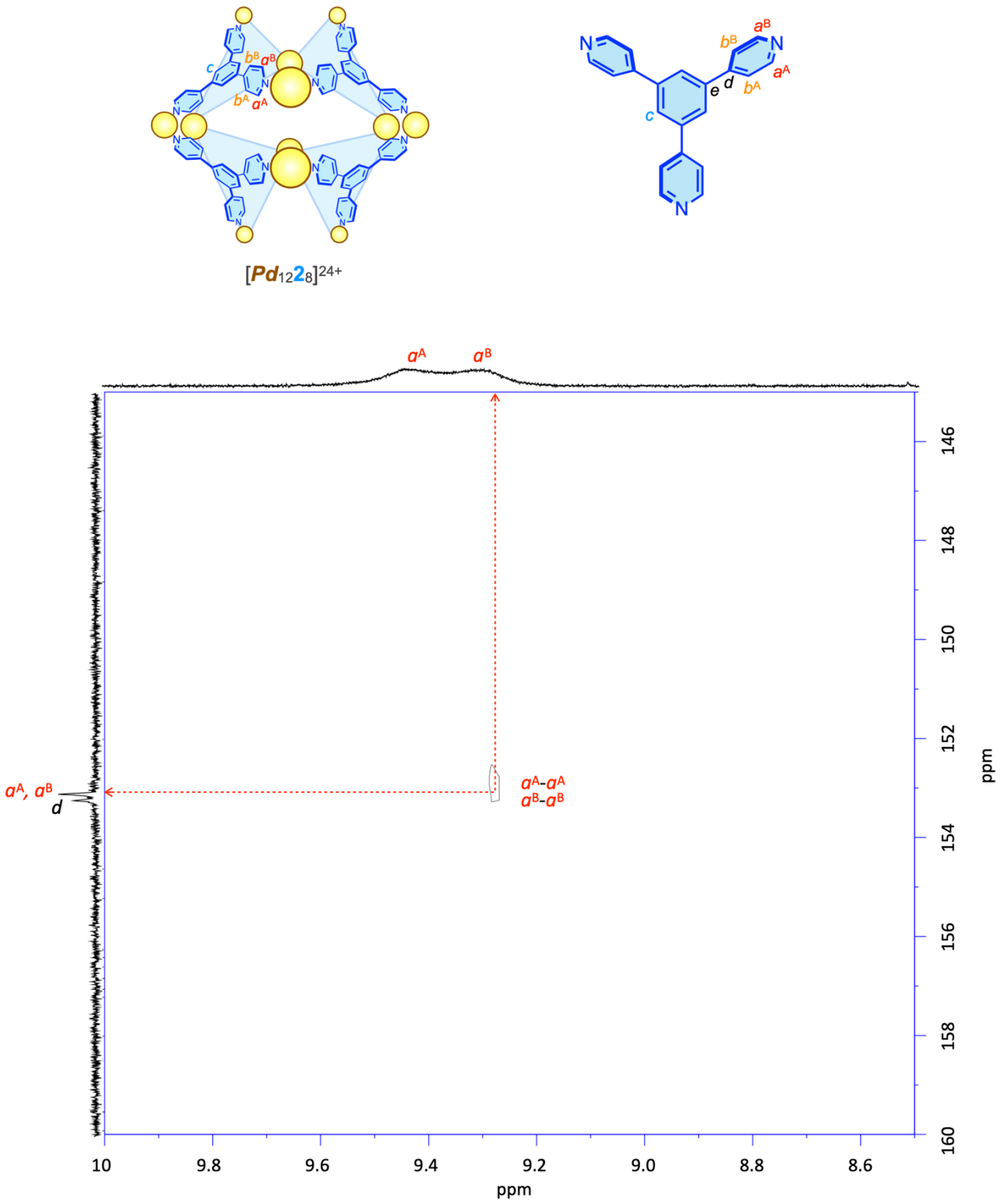

Supplementary Fig. 5. (Continued) Expanded HMQC spectrum of the $[\boldsymbol{Pd}_{12}\mathbf{2}_8]^{24+}$ open icosahedron (500 MHz, CD_3NO_2, 298 K).

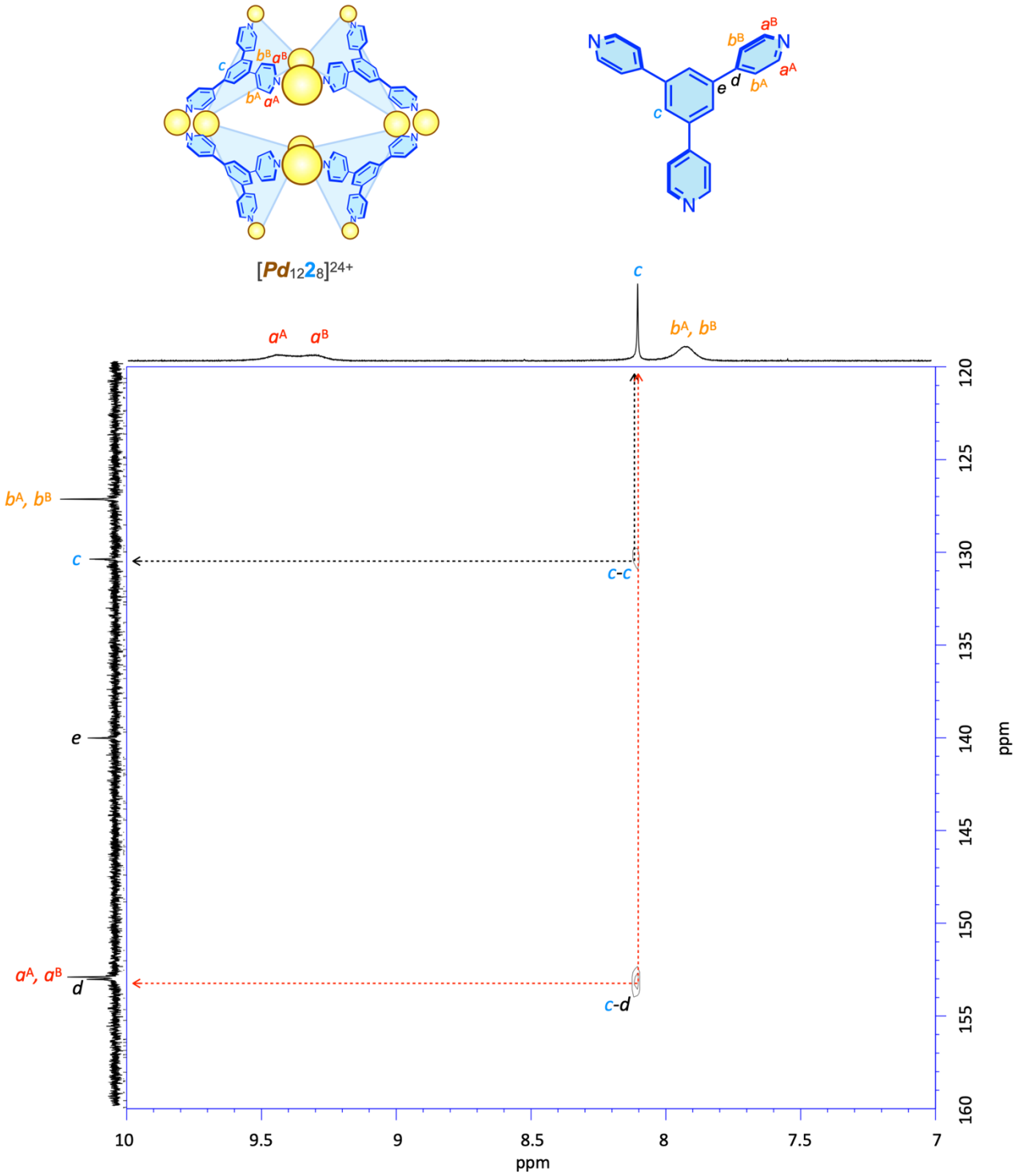

Supplementary Fig. 6. HMBC spectrum of the $[\boldsymbol{Pd}_{12}\boldsymbol{2}_8]^{24+}$ open icosahedron (500 MHz, CD_3NO_2, 298 K).

Characterization of the $[Pd_9\mathbf{2}_6]^{18+}$ open triaugmented triangular prism in solution

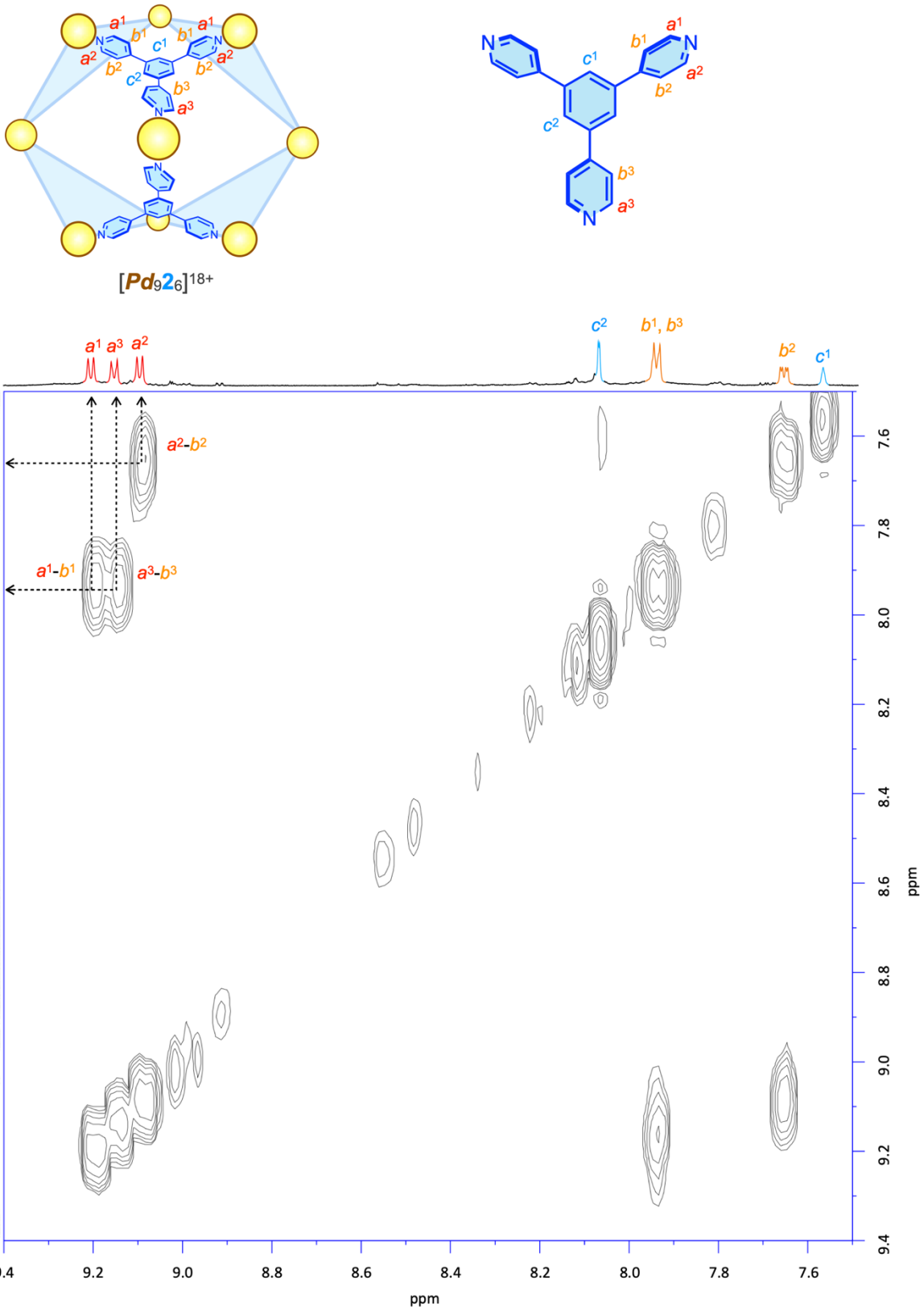

Supplementary Fig. 7. (H,H)-COSY spectrum of the $[Pd_9\mathbf{2}_6]^{18+}$ open triaugmented triangular prism (500 MHz, CD_3NO_2, 298 K).

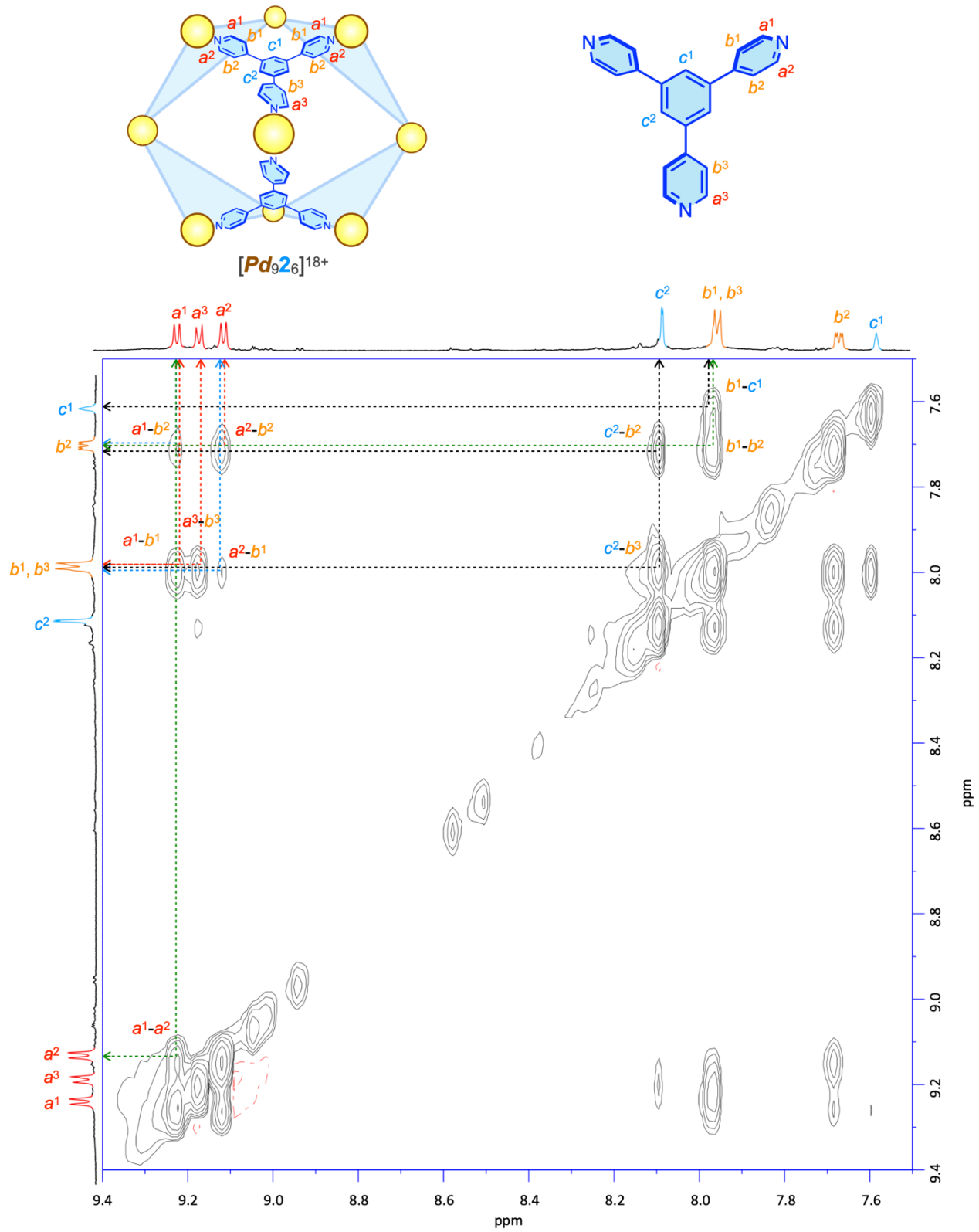

Supplementary Fig. 8. (H,H)-NOESY spectrum of the $[\mathbf{Pd}_9\mathbf{2}_6]^{18+}$ open triaugmented triangular prism (500 MHz, CD_3NO_2, 298 K).

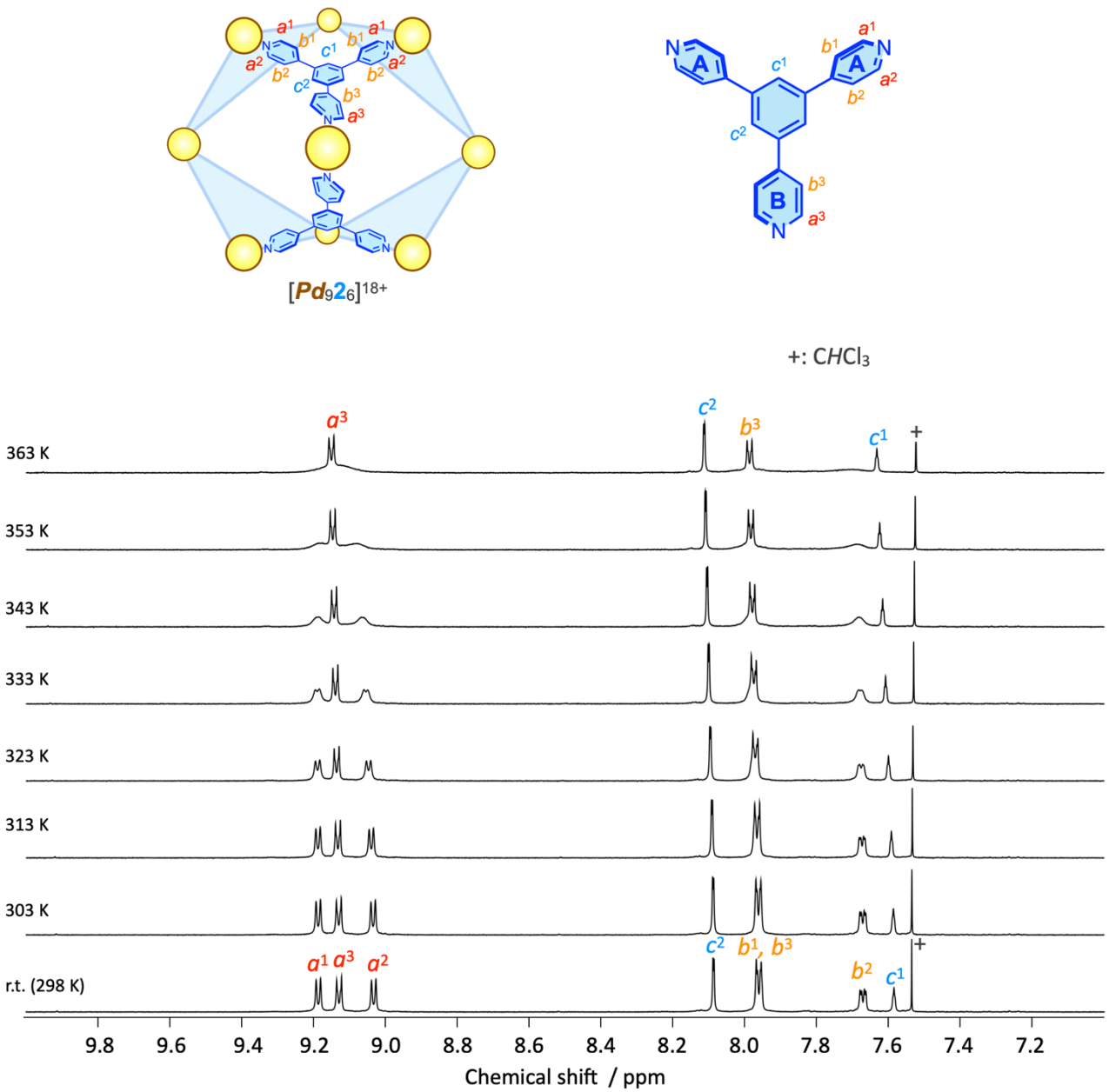

Supplementary Fig. 9. Variable-temperature ^{1}H NMR spectra of the [***Pd***$_9$**2**$_6$]$^{18+}$ open triaugmented triangular prism (500 MHz, CD_3NO_2). a^1, a^2, b^1, and b^2 signals coalesced at 363 K, indicating the rotation of the 4-pyridyl rings **A** comparable to the NMR time scale at 363 K. In contrast, c^1 and c^2 signals in the central benzene ring did not change at all, indicating the C_{2v} symmetry of the tritopic ligand **2** in the assembled structure, which is consistent with the [***Pd***$_9$**2**$_6$]$^{18+}$ open triaugmented triangular prism structure.

Conversion of $[Pd_9\mathbf{2}_6]^{18+}$ to $[Pd_{12}\mathbf{2}_8]^{24+}$ by heating

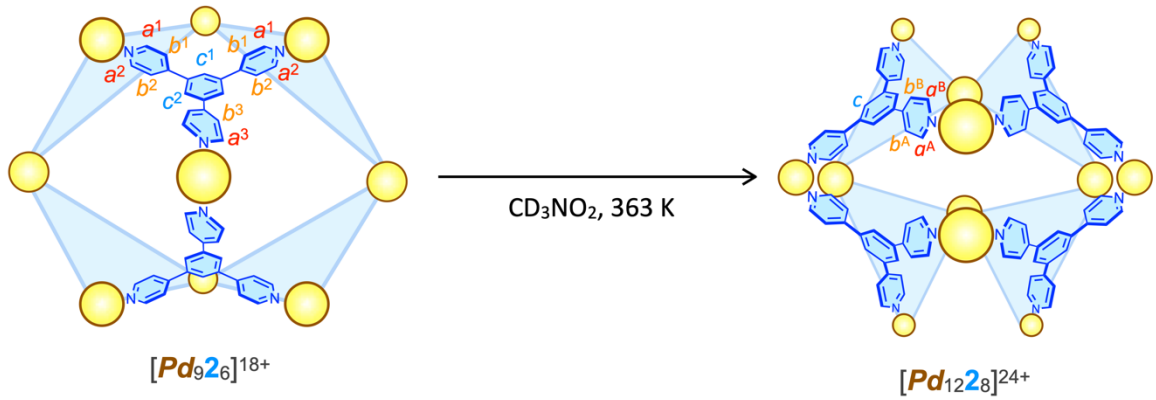

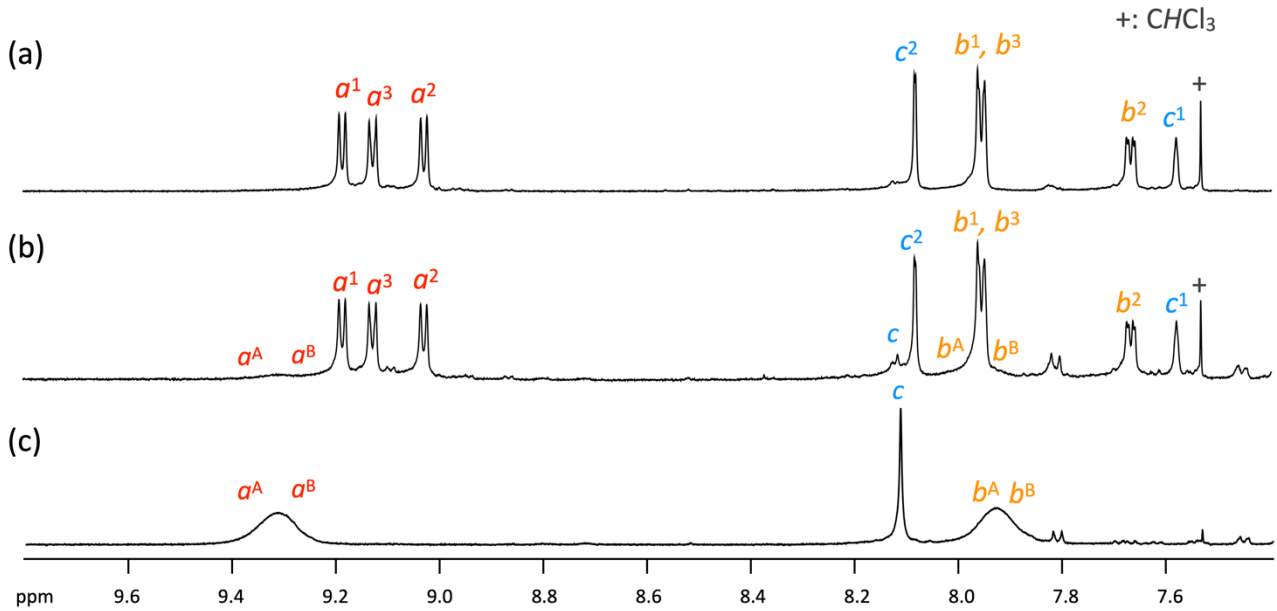

Supplementary Fig. 10. ^{1}H NMR spectra for the conversion of $[Pd_9\mathbf{2}_6]^{18+}$ to $[Pd_{12}\mathbf{2}_8]^{24+}$ (500 MHz, CD_3NO_2, 298 K). (a) $[Pd_9\mathbf{2}_6]^{18+}$ measured before heating. The NMR yield of $[Pd_9\mathbf{2}_6]^{18+}$ determined based on the internal standard ([2.2]paracyclophane) is 96%. (b) Heating a solution of $[Pd_9\mathbf{2}_6]^{18+}$ at 363 K for 2.5 days without NO_3^- caused the decrease in the yield of $[Pd_9\mathbf{2}_6]^{18+}$ (77%) and afforded $[Pd_{12}\mathbf{2}_8]^{24+}$ (8%). (c) In the presence of NO_3^- ($[Pd]_{total}/[NO_3^-]$ = 3:1), heating a solution of $[Pd_9\mathbf{2}_6]^{18+}$ at 363 K for 4 days afforded $[Pd_{12}\mathbf{2}_8]^{24+}$ in 84% yield.

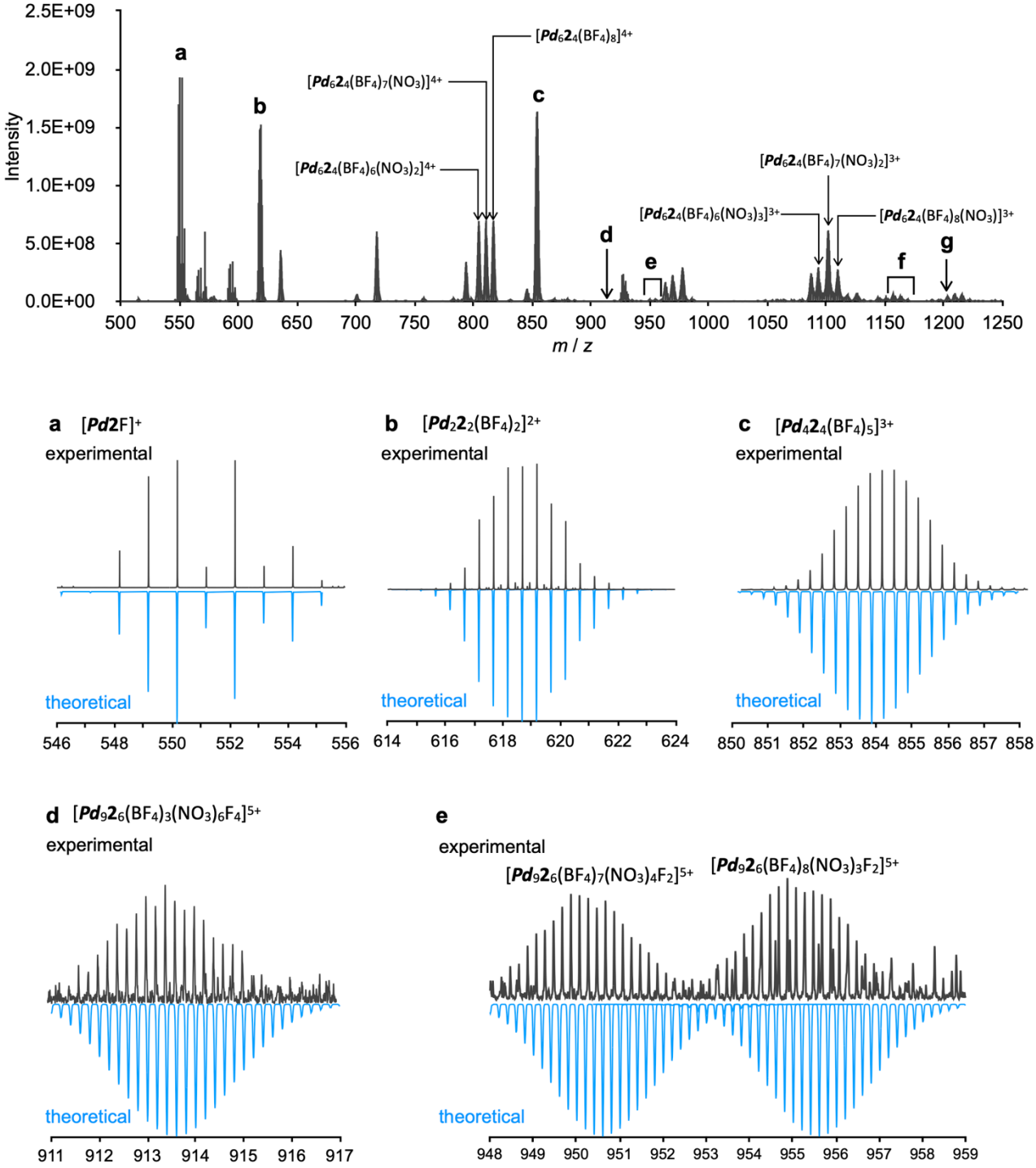

Supplementary Fig. 11. CSI FT-ICR MS spectra of the $[\boldsymbol{Pd}_9\boldsymbol{2}_6]^{18+}$ triaugmented triangular prism from $[\boldsymbol{Pd}(CH_3CN)_2](BF_4)_2$ and **2** in the presence of *n*-$Bu_4{\cdot}NNO_3$ in CH_3NO_2, diluted with CH_3NO_2. (a) $[\boldsymbol{Pd}\boldsymbol{2}F]^+$, (b) $[\boldsymbol{Pd}_2\boldsymbol{2}_2(BF_4)_2]^{2+}$, (c) $[\boldsymbol{Pd}_4\boldsymbol{2}_4(BF_4)_5]^{3+}$, (d) $[\boldsymbol{Pd}_9\boldsymbol{2}_6(BF_4)_3(NO_3)_6F_4]^{5+}$, (e) $[\boldsymbol{Pd}_9\boldsymbol{2}_6X_{13}]^{5+}$. X indicates counter anions (NO_3^-, BF_4^-, and F^-).

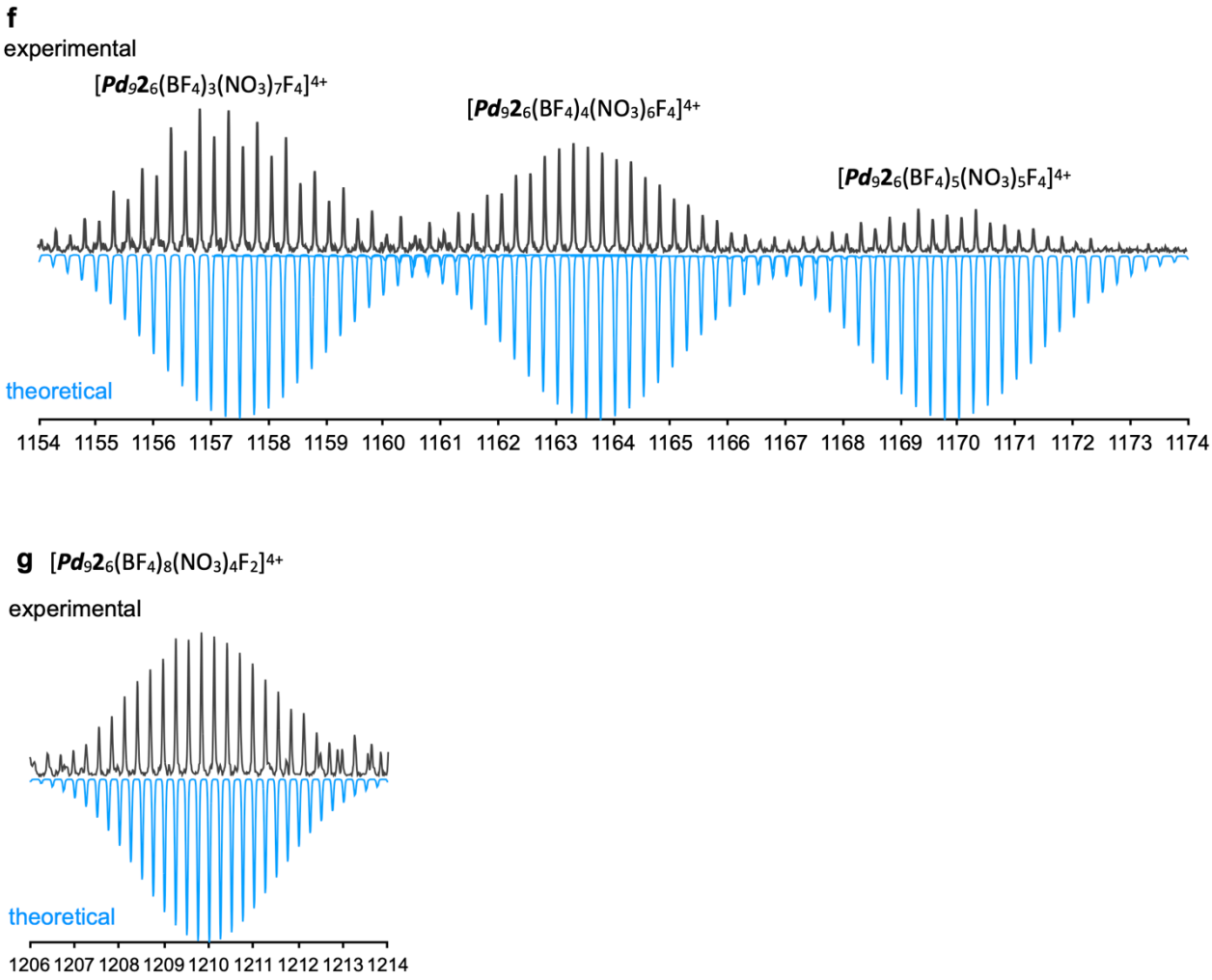

Supplementary Fig. 11. (Continued) CSI FT-ICR MS spectra of the $[\boldsymbol{Pd}_9\boldsymbol{2}_6]^{18+}$ triaugmented triangular prism from $[\boldsymbol{Pd}(CH_3CN)_2](BF_4)_2$ and **2** in the presence of *n*-$Bu_4N{\cdot}NO_3$ in CH_3NO_2, diluted with CH_3NO_2. (f) $[\boldsymbol{Pd}_9\boldsymbol{2}_6X_{14}]^{4+}$, and (g) $[\boldsymbol{Pd}_9\boldsymbol{2}_6(BF_4)_8(NO_3)_4F_2]^{4+}$. X indicates counter anions (NO_3^-, BF_4^-, and F^-).

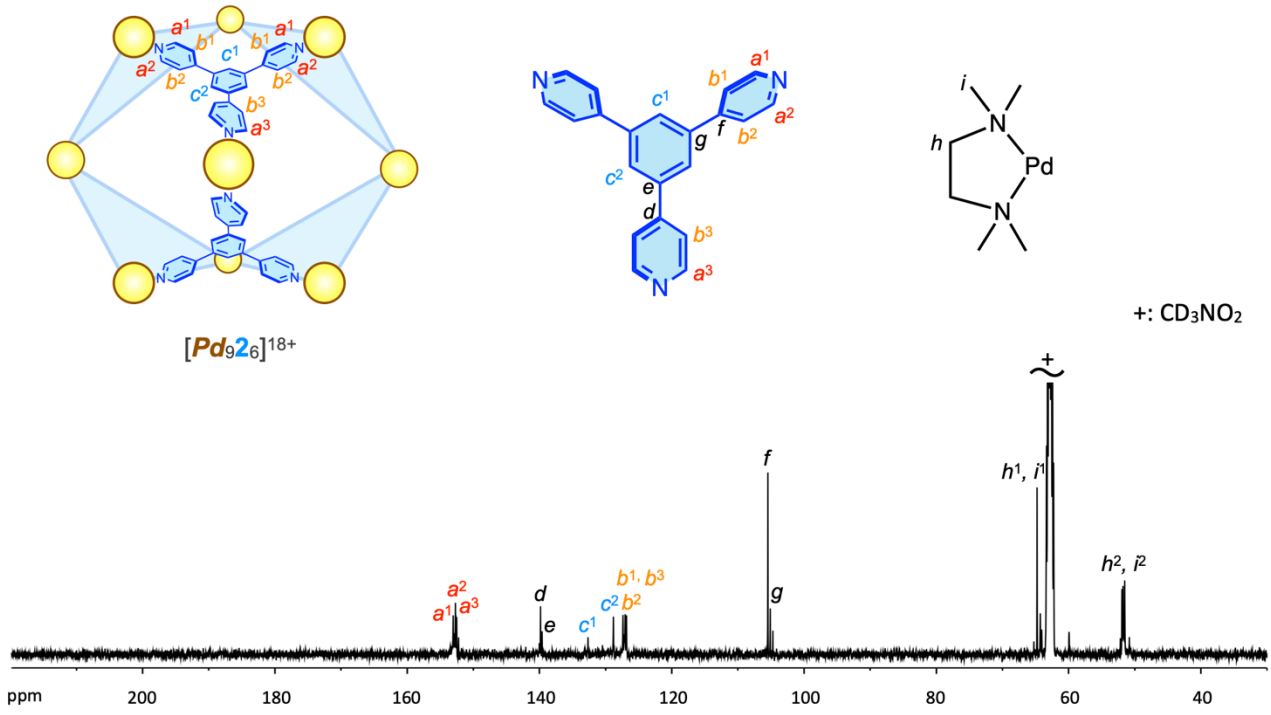

Supplementary Fig. 12. ^{13}C NMR spectrum of the [***Pd***$_9$**2**$_6$]$^{18+}$ open triaugmented triangular prism (125 MHz, CD_3NO_2, 298 K).

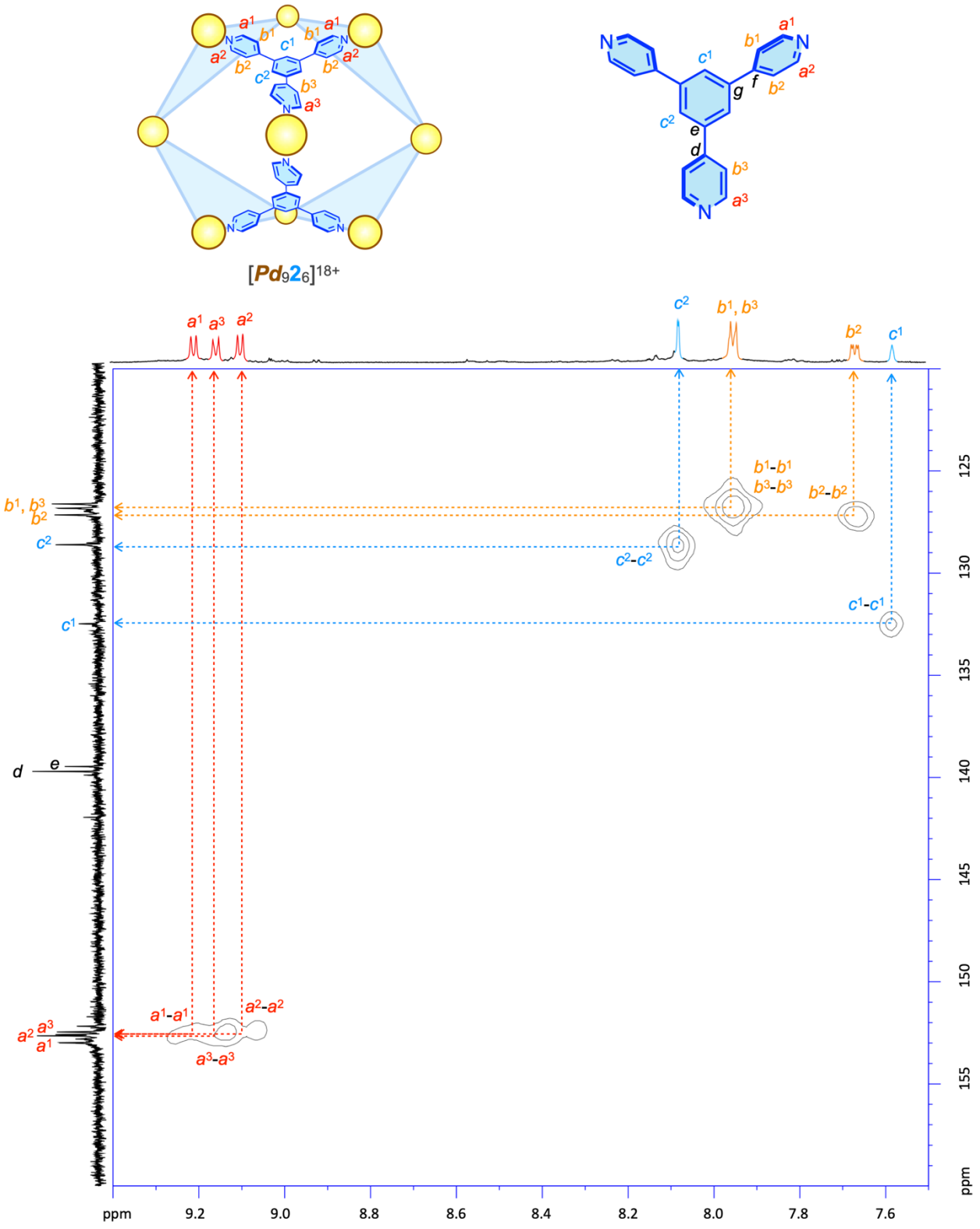

Supplementary Fig. 13. HMQC spectrum of the $[\boldsymbol{Pd}_9\boldsymbol{2}_6]^{18+}$ open triaugmented triangular prism (500 MHz, CD_3NO_2, 298 K).

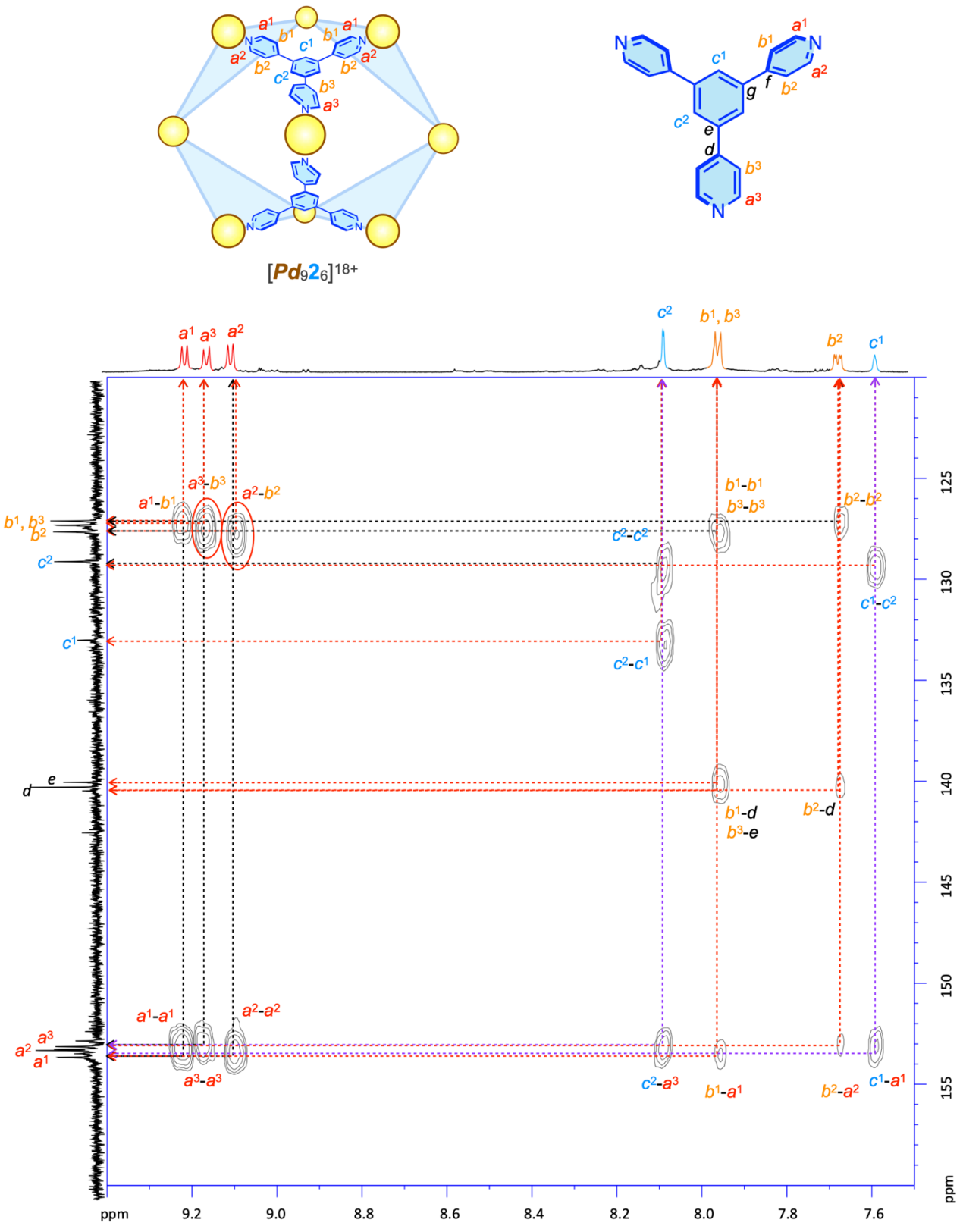

Supplementary Fig. 14. HMBC spectrum of the $[\boldsymbol{Pd}_9\boldsymbol{2}_6]^{18+}$ open triaugmented triangular prism (500 MHz, CD_3NO_2, 298 K).

Energy-minimized structures of [*Pd*$_6$2**$_4$]$^{12+}$, [*Pd*$_9$**2**$_6$]$^{18+}$, and [*Pd*$_{12}$**2**$_8$]$^{24+}$**

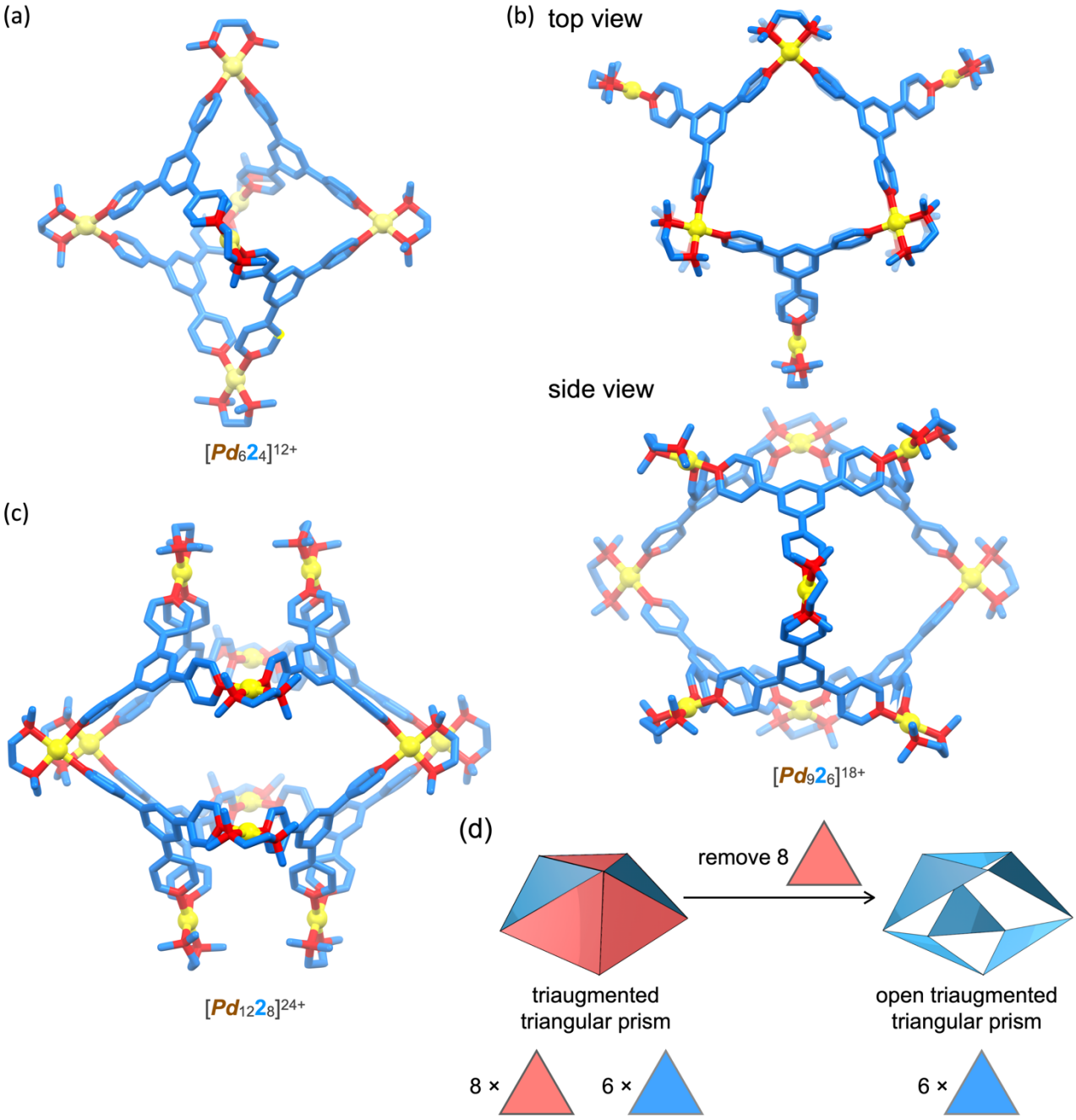

Supplementary Fig. 15. DFT-optimized structures of (a) the [*Pd*$_6$**2**$_4$]$^{12+}$ open octahedron, (b) the [*Pd*$_9$**2**$_6$]$^{18+}$ open triaugmented triangular prism, and (c) the [*Pd*$_{12}$**2**$_8$]$^{24+}$ open icosahedron using B3LYP/def2-SV(P) level of theory. Color labels: Yellow = Pd; Blue = C; Red = N. Hydrogen atoms and counter anions (BF_4^-) are omitted for clarity. (d) Schematic representation of the geometry of the [*Pd*$_9$**2**$_6$]$^{18+}$ open triaugmented triangular prism. 8 regular triangles in red shown in the triaugmented triangular prism are removed to form an open triaugmented triangular prism, where the 6 regular triangle in blue correspond to tritopic ligand **2** in [*Pd*$_9$**2**$_6$]$^{18+}$. 9 *cis*-protected ions (*Pd*$^{2+}$) on the apexes are omitted.

The effect of the *cis*-protecting group in the self-assembly

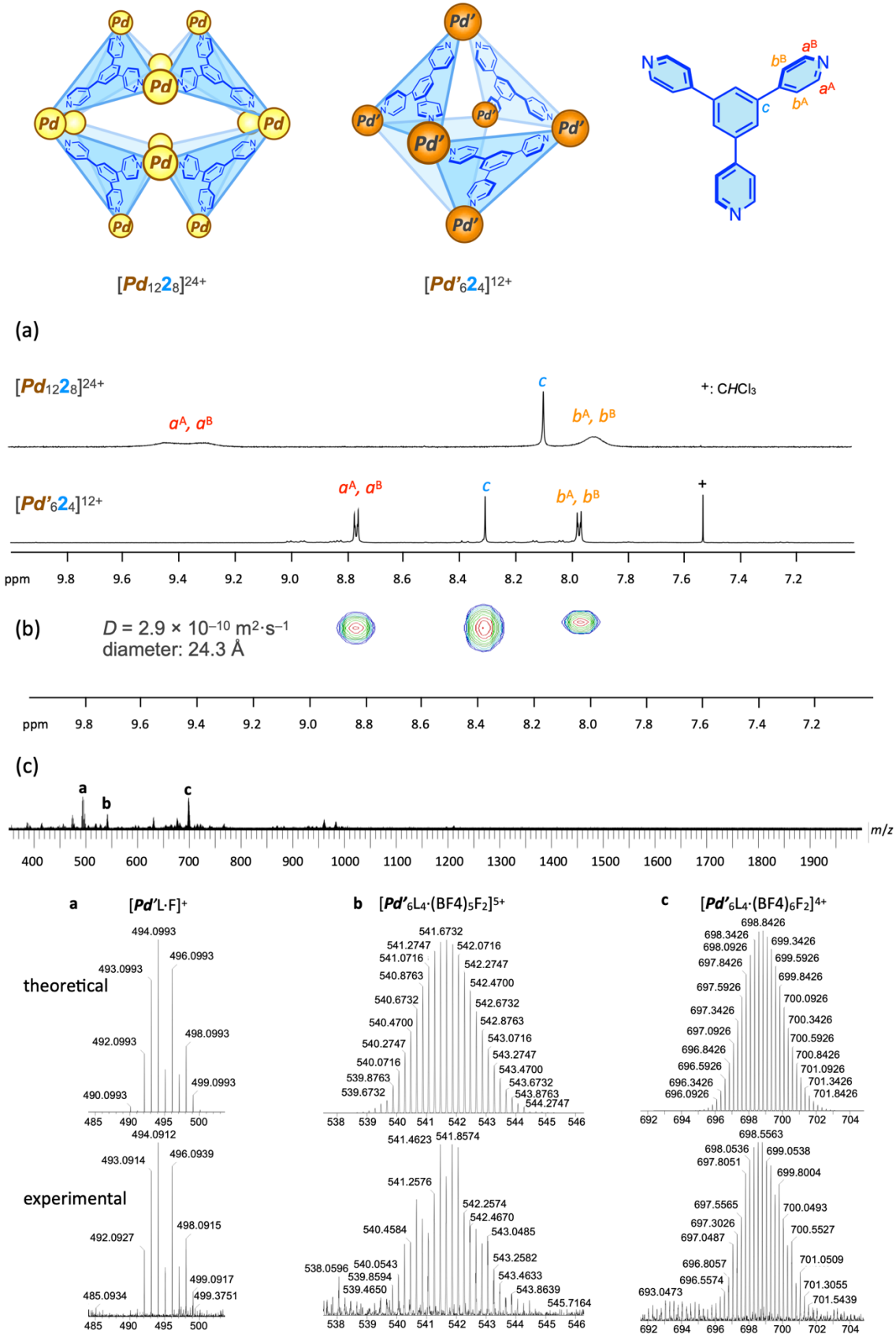

Supplementary Fig. 16. Characterization of the $[\boldsymbol{Pd'}_6\mathbf{2}_4]^{12+}$ open octahedron. ***Pd'*** indicates Pd(en). (a) ^{1}H NMR spectrum for the self-assembly of tritopic ligand **2** and $\boldsymbol{Pd'}^{2+}$ (500 MHz, CD_3NO_2, 298 K). ^{1}H NMR spectrum of the $[\boldsymbol{Pd}_{12}\mathbf{2}_8]^{24+}$ open icosahedron is shown for comparison. (b) ^{1}H DOSY spectrum of the $[\boldsymbol{Pd'}_6\mathbf{2}_4]^{12+}$ open octahedron. (c) ESI-TOF mass spectrum of $[\boldsymbol{Pd'}_6\mathbf{2}_4]^{12+}$.

(d)

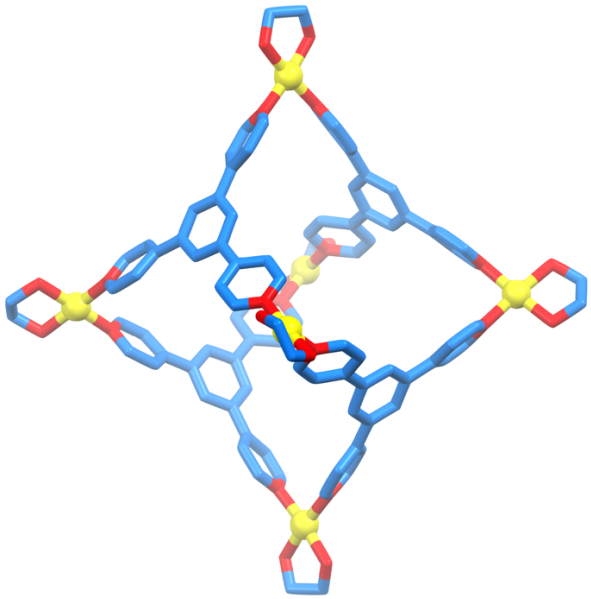

$[\boldsymbol{Pd'}_6\mathbf{2}_4]^{12+}$

Supplementary Fig. 16. (Continued) Characterization of the $[\boldsymbol{Pd'}_6\mathbf{2}_4]^{12+}$ open octahedron. ***Pd'*** indicates Pd(en). (d) DFT-optimized structure of $[\boldsymbol{Pd'}_6\mathbf{2}_4]^{12+}$ using B3LYP/def2-SV(P) level of theory. Color labels: Yellow = Pd; Blue = C; Red = N. Hydrogen atoms and counter anions (BF_4^-) are omitted for clarity. The average ϑ and φ value of **2** in $[\boldsymbol{Pd'}_6\mathbf{2}_4]^{12+}$ is 27.5±1.5° and 70.9±7.2°, respectively. The largely smaller φ value than the ideal value (90°) indicates that the strain in $[\boldsymbol{Pd'}_6\mathbf{2}_4]^{12+}$ caused by ϑ around 30° is relieved by decreasing in φ, diminishing the remote geometric communication.

Self-assembly of 2 with [Zn(TMEDA)]$^{2+}$

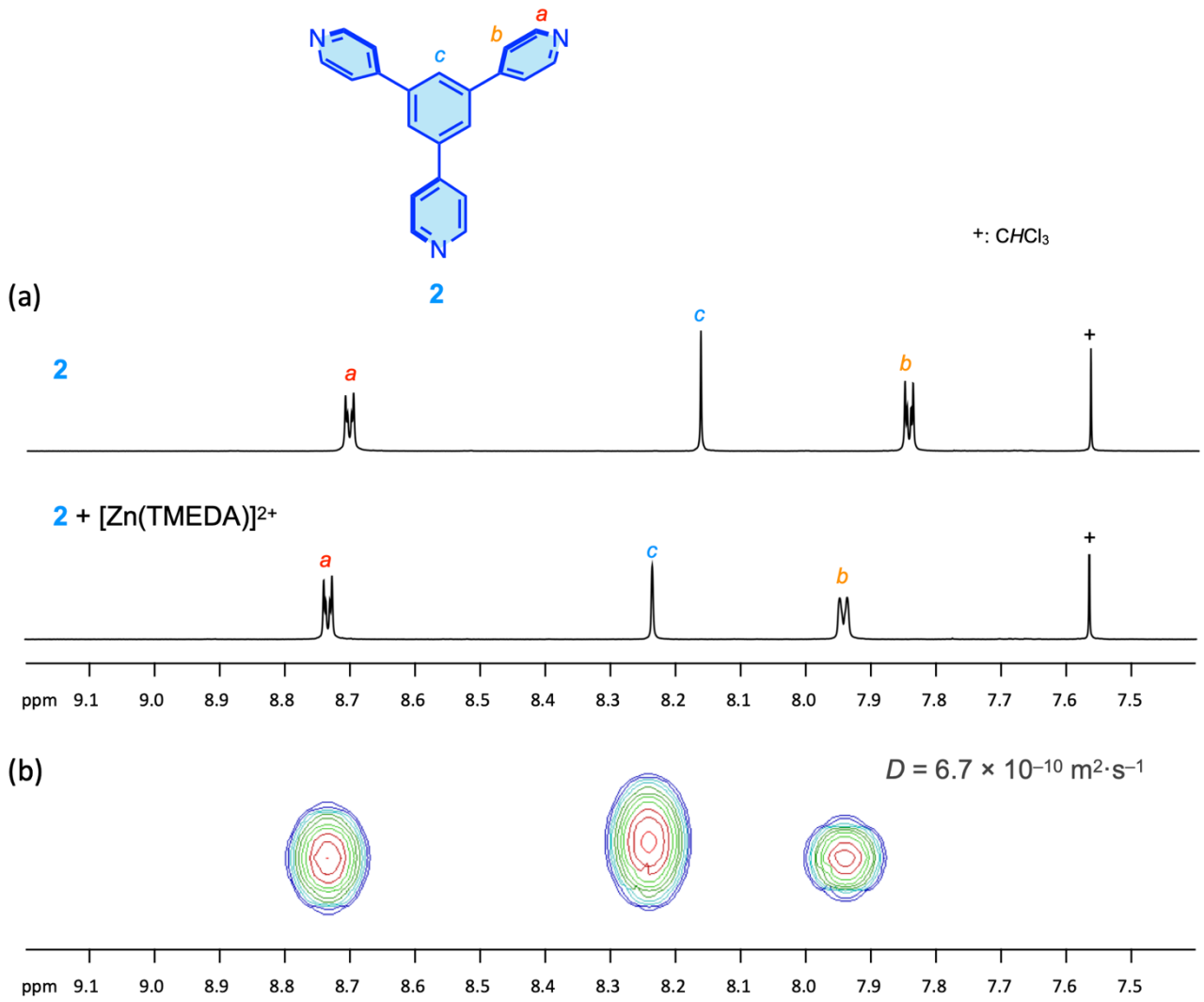

Supplementary Fig. 17. ^{1}H NMR spectrum for the self-assembly of tritopic ligand **2** and [Zn(TMEDA)]$^{2+}$ in a 2:3 ratio (500 MHz, $CD_3NO_2/CDCl_3/CD_3OD$ = 7/3/2 (*v*/*v*/*v*), 298 K). (a) ^{1}H NMR spectrum of a mixture of **2** and [Zn(TMEDA)]$^{2+}$ in a 2:3 ratio. ^{1}H NMR spectrum of free **2** is shown for comparison. (b) ^{1}H DOSY spectrum of a mixture of **2** and [Zn(TMEDA)]$^{2+}$ in a 2:3 ratio.

Self-assembly of the $[Pd_2\mathbf{3}_2]^{4+}$ ring

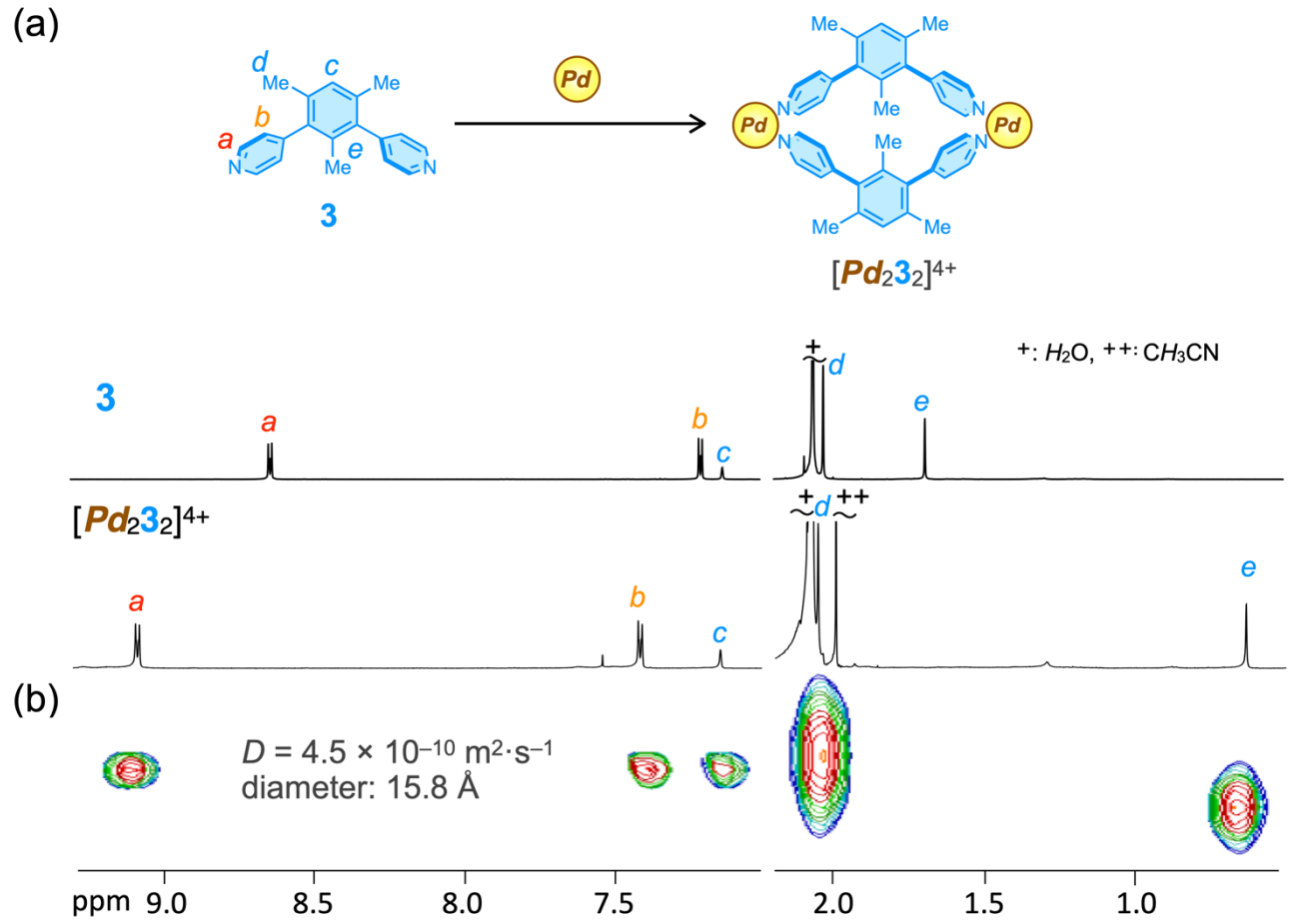

Supplementary Fig. 18. Self-assembly of the $[Pd_2\mathbf{3}_2]^{4+}$ ring from ditopic ligand **3** and Pd^{2+} in a 1:1 ratio. (a) ^{1}H NMR spectrum of the $[Pd_2\mathbf{3}_2]^{4+}$ ring (500 MHz, CD_3NO_2, 298 K). The ^{1}H NMR spectrum of free **3** is shown for comparison. (b) ^{1}H DOSY spectrum of the $[Pd_2\mathbf{3}_2]^{4+}$ ring (500 MHz, CD_3NO_2, 298 K).

Self-assembly of 4 and *Pd*$^{2+}$

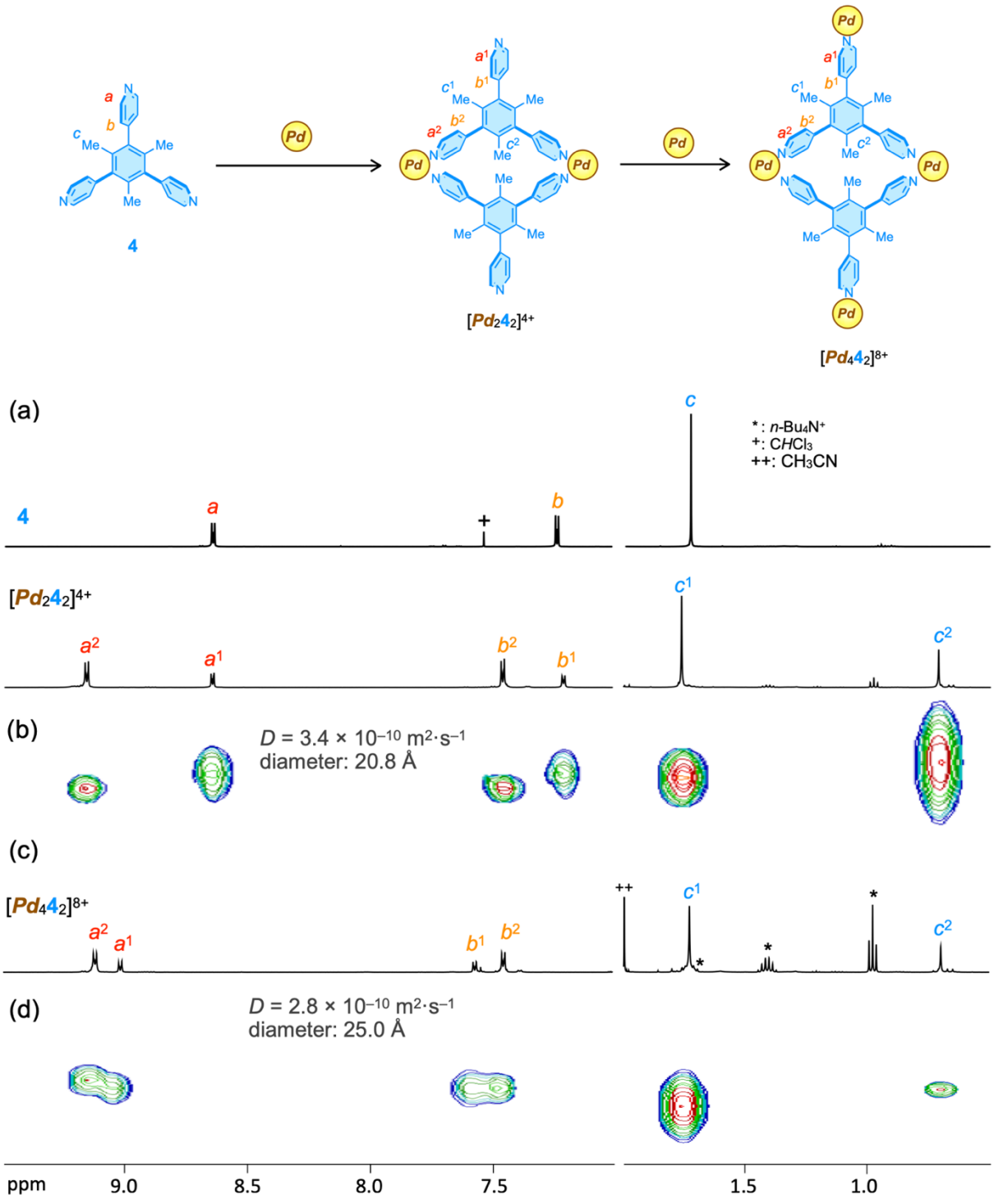

Supplementary Fig. 19. ^{1}H NMR for the self-assembly of **4** and ***Pd***$^{2+}$ (500 MHz, CD_3NO_2, 298 K). (a) A mixture of **4** and ***Pd***$^{2+}$ in a 1:1 ratio. The ^{1}H NMR spectrum of free **4** is shown for comparison. (b) ^{1}H DOSY spectrum of a mixture of **4** and ***Pd***$^{2+}$ in a 1:1 ratio. (c) Addition of 2 equiv. of ***Pd***$^{2+}$ to the solution of $[\boldsymbol{Pd}_2\boldsymbol{4}_2]^{4+}$ to form $[\boldsymbol{Pd}_4\boldsymbol{4}_2]^{4+}$ (d) ^{1}H DOSY spectrum of the solution obtained in (c), a solution of **4** and ***Pd***$^{2+}$ in a 1:2 ratio to form $[\boldsymbol{Pd}_4\boldsymbol{4}_2]^{8+}$, where residual H_2O in the solvent, CH_3CN (leaving ligand of the metal source), or BF_4^- would coordinate to the outer Pd(II) centers under faster exchange than the NMR time scale. When **4** and ***Pd***$^{2+}$ were mixed in a 3:2 ratio, precipitation occurred, suggesting the formation of oligomers of $[\boldsymbol{Pd}_{3n}\boldsymbol{4}_{2n}]^{6+}$ consisting of the $[\boldsymbol{Pd}_2\boldsymbol{4}_2]^{4+}$ rings connected by ***Pd***$^{2+}$.

Characterization of the $[Pd_4\mathbf{4}_2]^{8+}$ ring

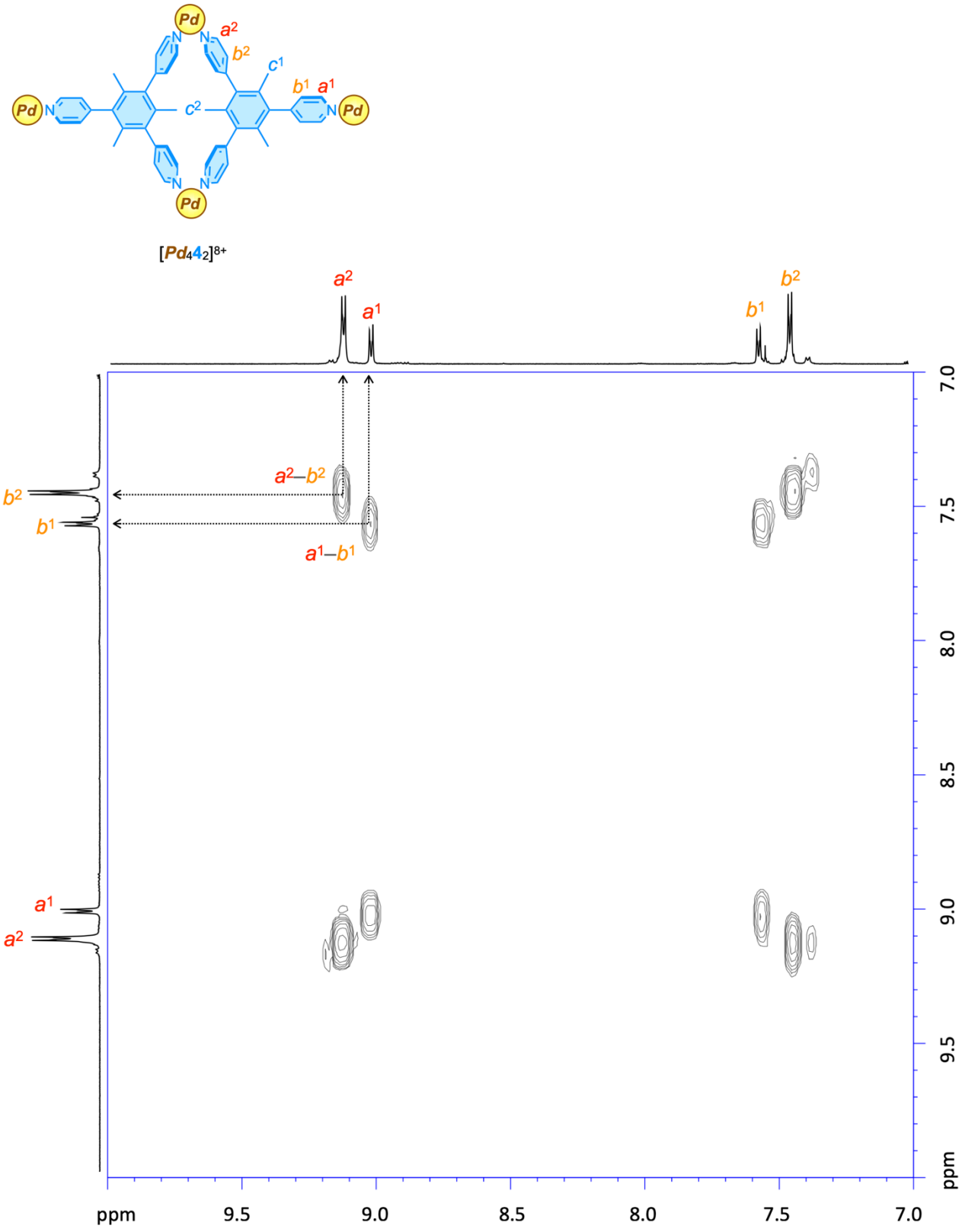

Supplementary Fig. 20. (H,H)-COSY spectrum of the $[Pd_4\mathbf{4}_2]^{8+}$ ring (500 MHz, CD_3NO_2, 298 K).

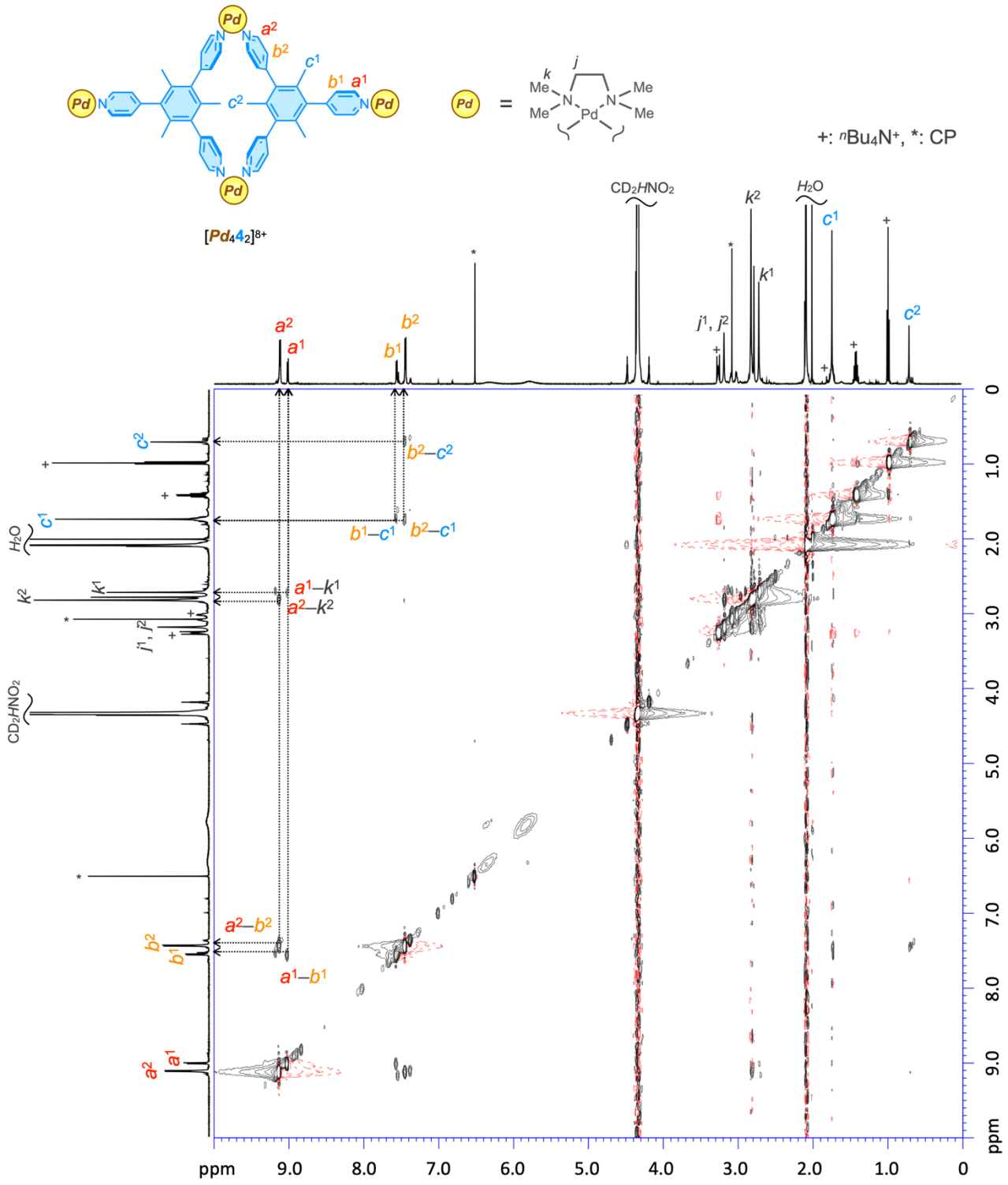

Supplementary Fig. 21. (H,H)-NOESY spectrum of the $[\boldsymbol{Pd}_4\boldsymbol{4}_2]^{8+}$ ring (500 MHz, CD_3NO_2, 298 K). The signals indicated by asterisk were assigned to [2.2]paracyclophane (CP), which was included as the internal standard to determine the yield.

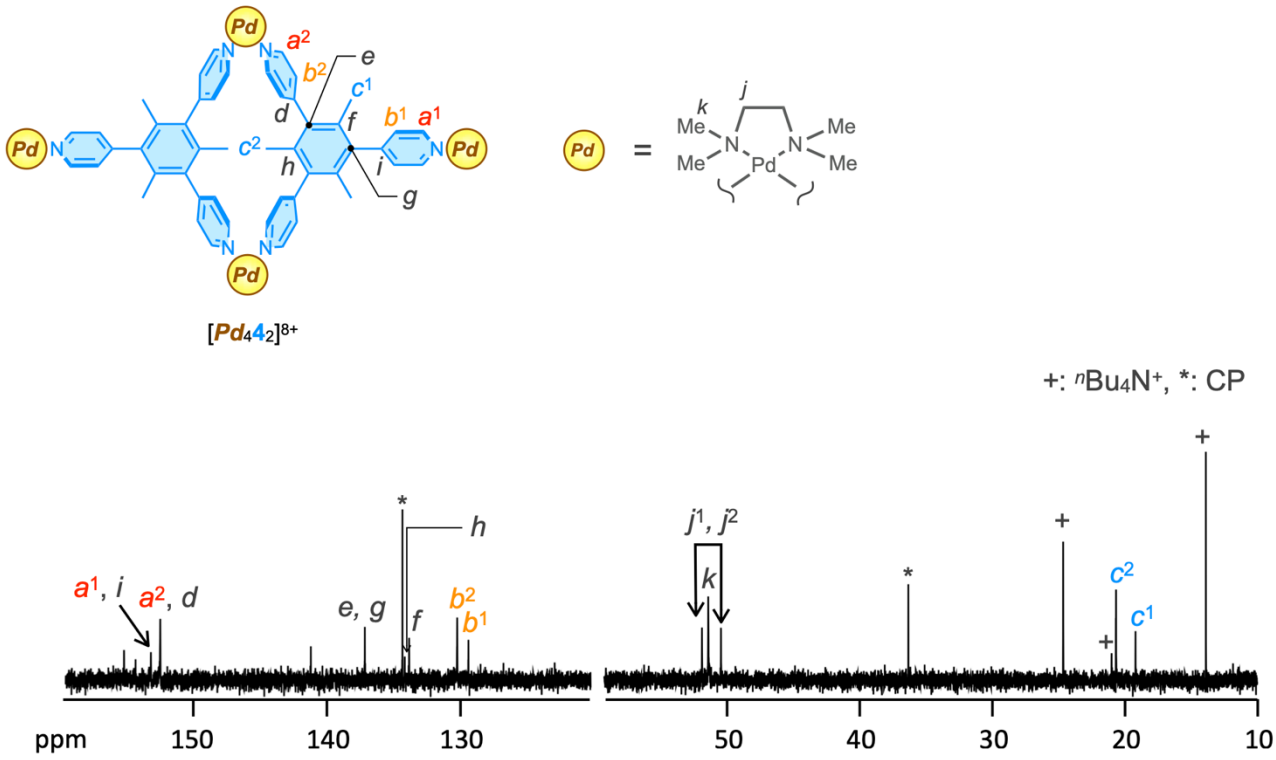

Supplementary Fig. 22. ^{13}C NMR spectrum of the $[\boldsymbol{Pd_4L_2}]^{8+}$ ring (125 MHz, CD_3NO_2, 298 K). The assignment of the signals was conducted based on HSQC and HMBC spectra (Supplementary Figures 23 and 24). The signals indicated by asterisk were assigned to [2.2]paracyclophane (CP), which was included as the internal standard to determine the yield.

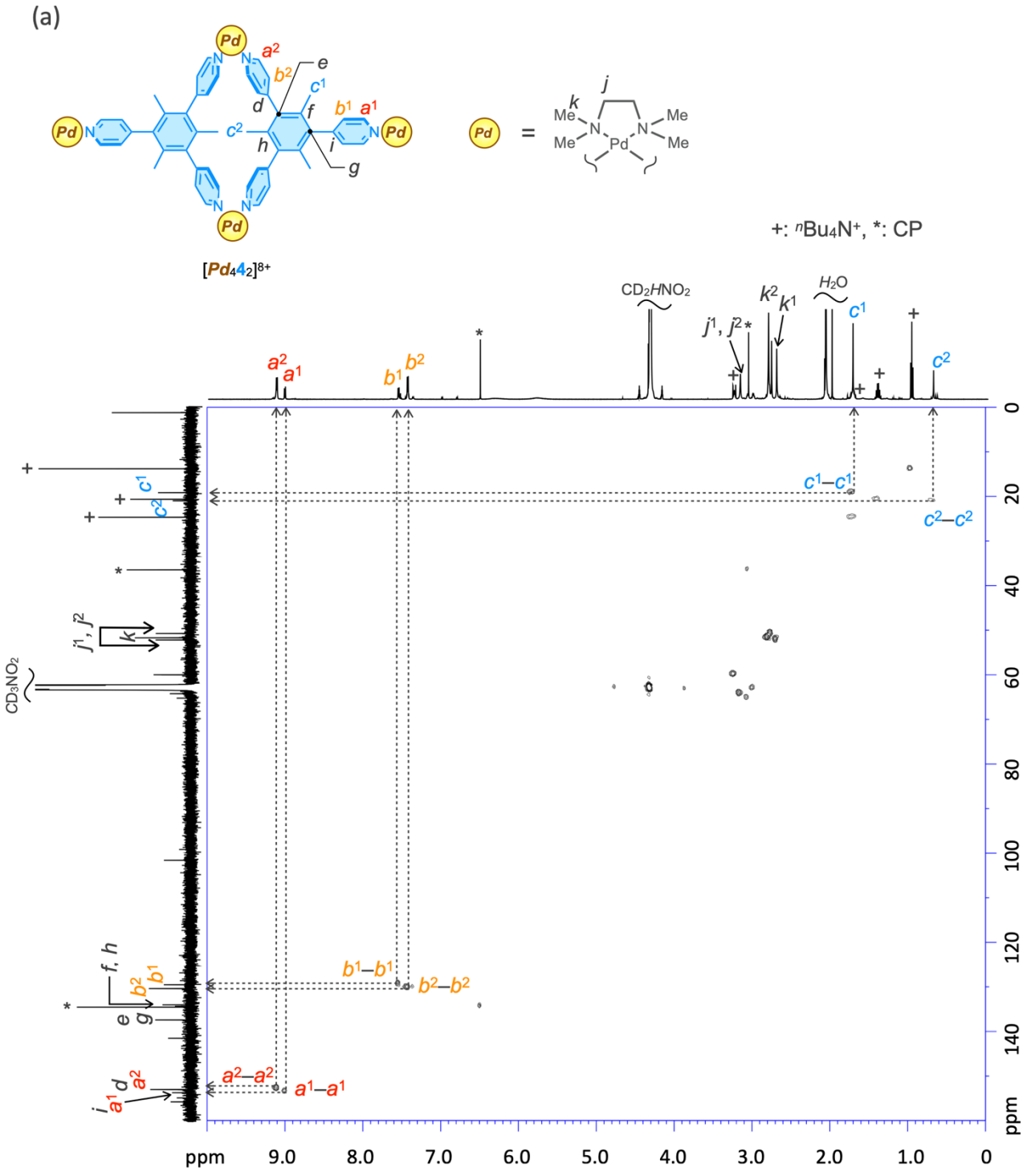

Supplementary Fig. 23. HSQC spectrum of the [***Pd***$_4$**4**$_2$]$^{8+}$ ring (500 MHz, CD_3NO_2, 298 K). (a) overall region in ^{1}H and ^{13}C spectra.

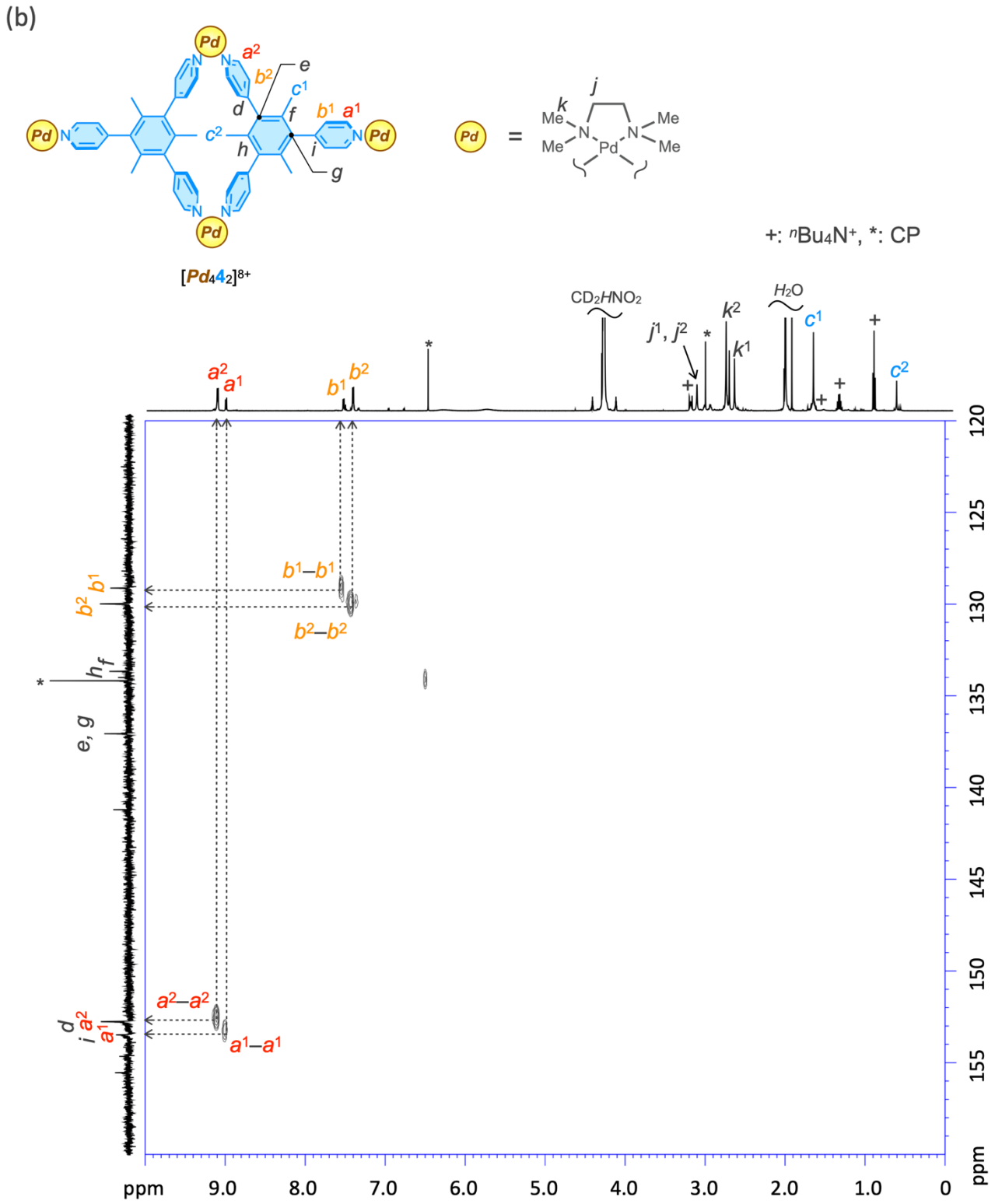

Supplementary Fig. 23. (continued) HSQC spectrum of the $[\boldsymbol{Pd_4L_2}]^{8+}$ ring (500 MHz, CD_3NO_2, 298 K). (b) overall region in the ^1H spectrum and aromatic region in the ^{13}C spectrum. The signals indicated by asterisk were assigned to [2.2]paracyclophane (CP), which was included as the internal standard to determine the yield.

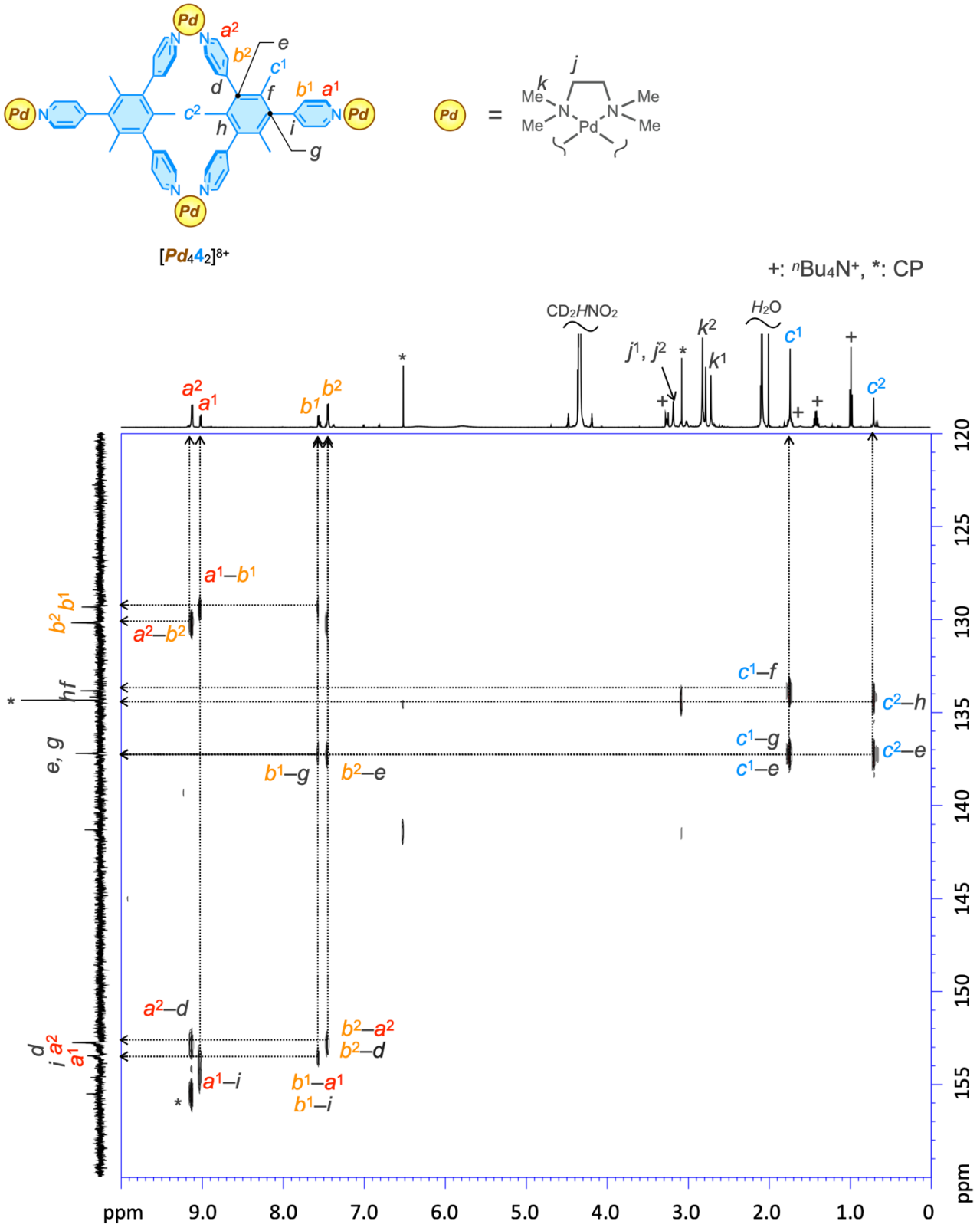

Supplementary Fig. 24. HMBC spectrum of the $[\boldsymbol{Pd_4L_2}]^{8+}$ ring (500 MHz, CD_3NO_2, 298 K). The signals indicated by asterisk were assigned to [2.2]paracyclophane (CP), which was included as the internal standard to determine the yield.

Energy-minimized structure of the $[M_{12}4_8]^{24+}$ square sheet

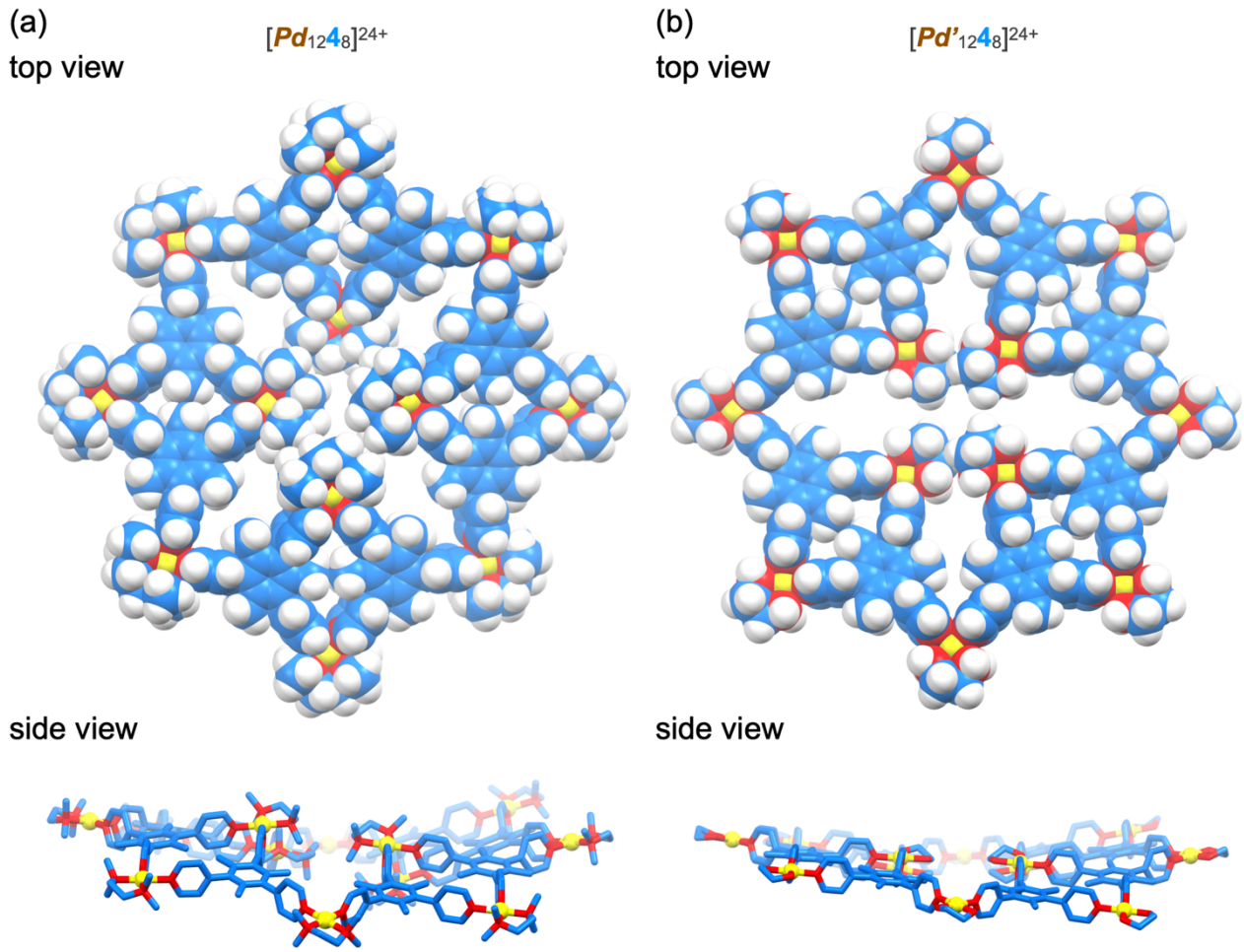

Supplementary Fig. 25. Energy-minimized structure of the $[\boldsymbol{M}_{12}\mathbf{4}_8]^{24+}$ square sheet by molecular mechanics calculation (***M***: ***Pd*** or ***Pd'***). Color labels: Yellow = Pd; Blue = C; Red = N, White = H. (a) The $[\boldsymbol{Pd}_{12}\mathbf{4}_8]^{24+}$ square sheet. (b) The $[\boldsymbol{Pd'}_{12}\mathbf{4}_8]^{24+}$ square sheet. Side views are shown as a cylinder model without hydrogen atoms for clarity. The planarity of the $[\boldsymbol{Pd}_{12}\mathbf{4}_8]^{24+}$ square sheet is poor because of the steric repulsion between TMEDA groups gathered in the center of the molecule, which would be the reason why a mixture of **4** and $\boldsymbol{Pd}^{2+}$ in a 3:2 ratio afforded precipitation of chain oligomers, whereas a mixture of **4** and $\boldsymbol{Pd'}^{2+}$ afforded a clear solution corresponding to the $[\boldsymbol{Pd'}_{12}\mathbf{4}_8]^{24+}$ square sheet (Fig. 7f and g).

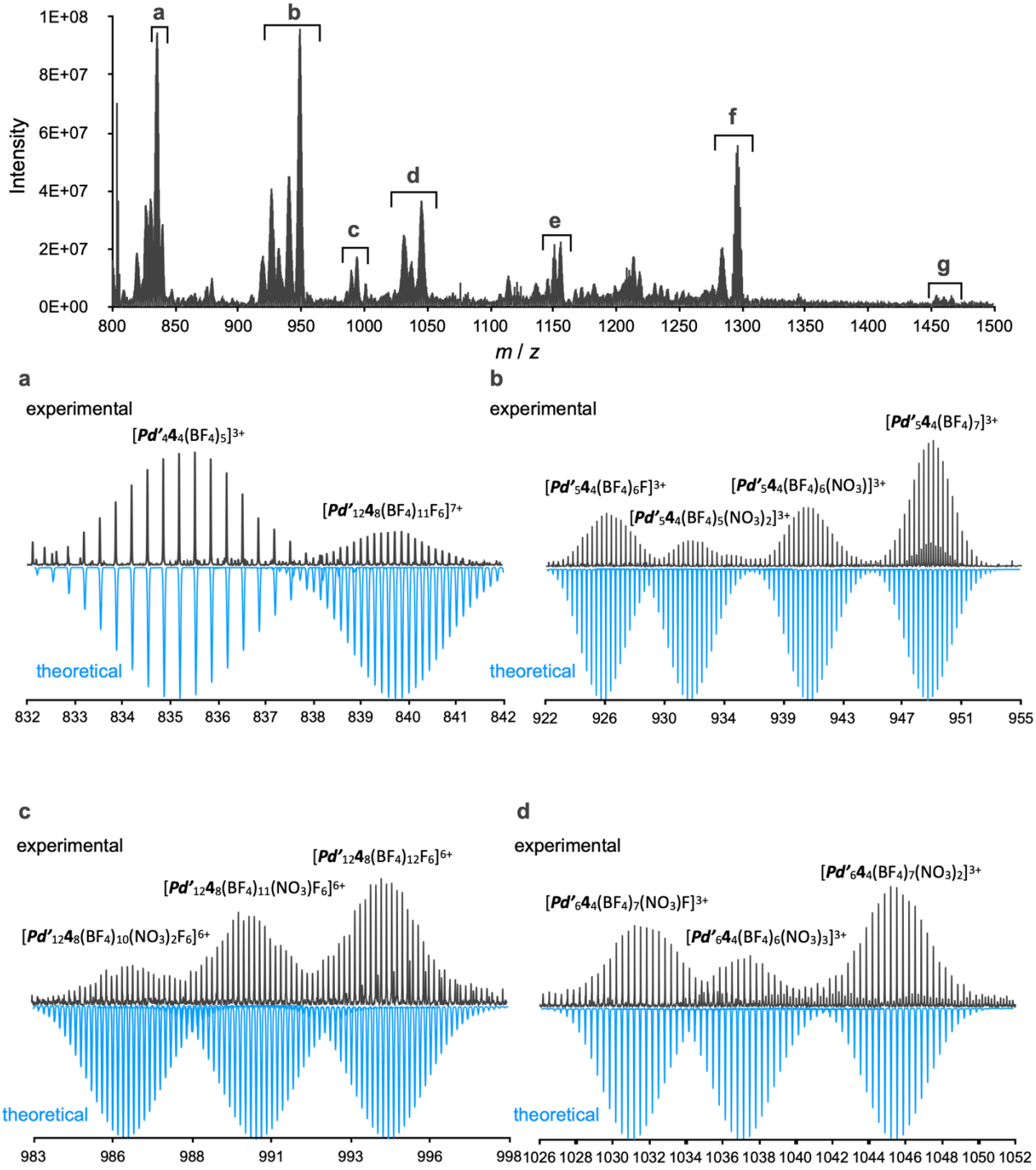

Supplementary Fig. 26. CSI FT-ICR MS spectra of the $[\boldsymbol{Pd'}_{12}\boldsymbol{4}_8]^{24+}$ square sheet from $[\boldsymbol{Pd'}(CH_3CN)_2](BF_4)_2$ and **4** in the presence of ^{n}Bu$_4$N·NO$_3$ in CD_3NO_2, diluted with CH_3NO_2. (a) $[\boldsymbol{Pd'}_4\boldsymbol{4}_4(BF_4)_5]^{3+}$ and $[\boldsymbol{Pd'}_{12}\boldsymbol{4}_8(BF_4)_{11}F_6]^{7+}$, (b) $[\boldsymbol{Pd'}_5\boldsymbol{4}_4X_7]^{3+}$, (c) $[\boldsymbol{Pd'}_{12}\boldsymbol{4}_8X_{18}]^{6+}$, and (d) $[\boldsymbol{Pd'}_6\boldsymbol{4}_4X_9]^{3+}$ species. X indicates counter anions (NO_3^-, BF_4^-, and F^-).

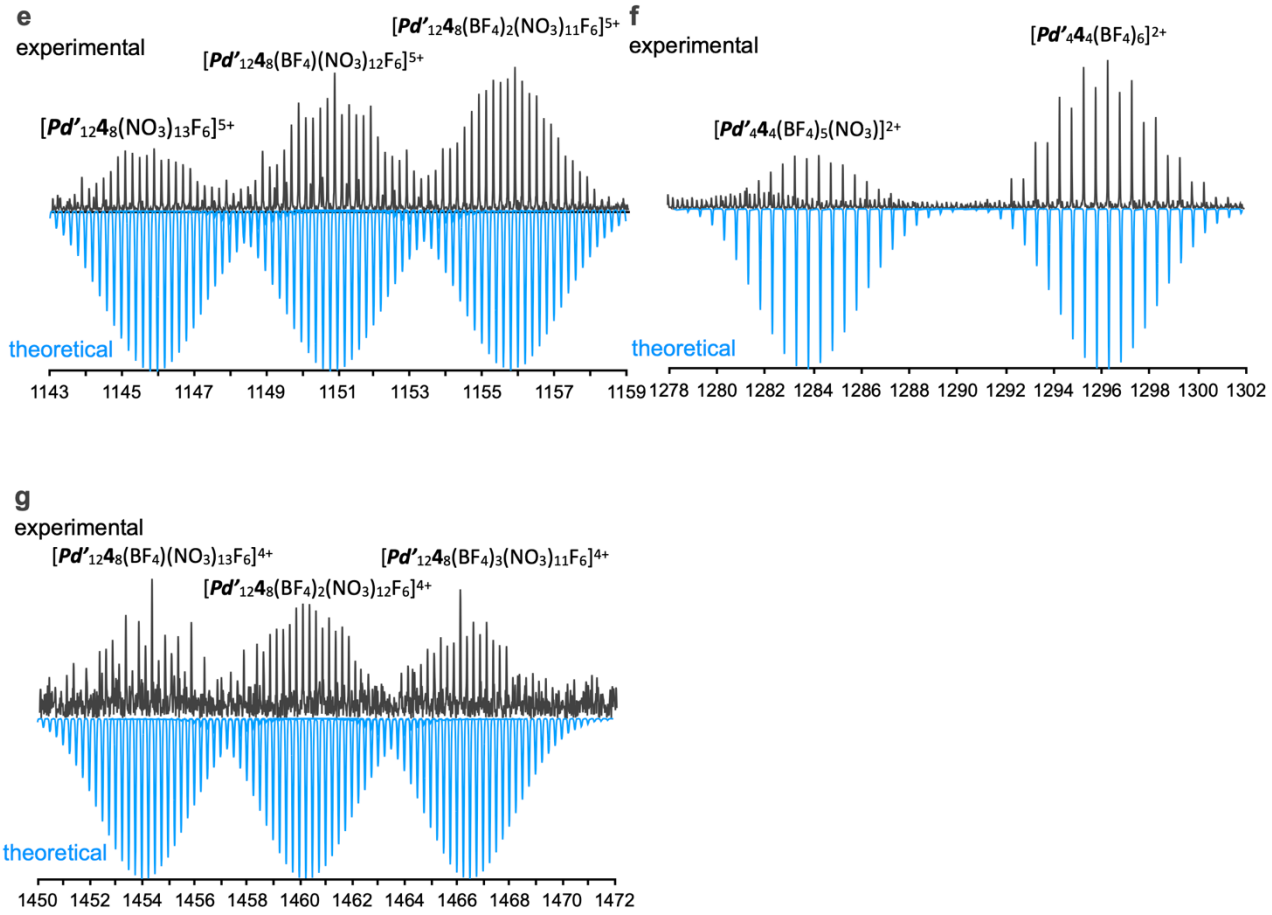

Supplementary Fig. 26. (continued) CSI FT-ICR MS spectra of the $[\boldsymbol{Pd'}_{12}\boldsymbol{4}_8]^{24+}$ square sheet from $[\boldsymbol{Pd'}(CH_3CN)_2](BF_4)_2$ and **4** in the presence of $^n Bu_4N{\cdot}NO_3$ in CD_3NO_2, diluted with CH_3NO_2. (e) $[\boldsymbol{Pd'}_{12}\boldsymbol{4}_8X_{19}]^{5+}$, (f) $[\boldsymbol{Pd'}_4\boldsymbol{4}_4X_6]^{2+}$, and (g) $[\boldsymbol{Pd'}_{12}\boldsymbol{4}_8\ X_{20}]^{4+}$. X indicates counter anions (NO_3^-, BF_4^-, and F^-).

Characterization of the [*Pd'*$_{12}$4**$_8$]$^{24+}$ square sheet**

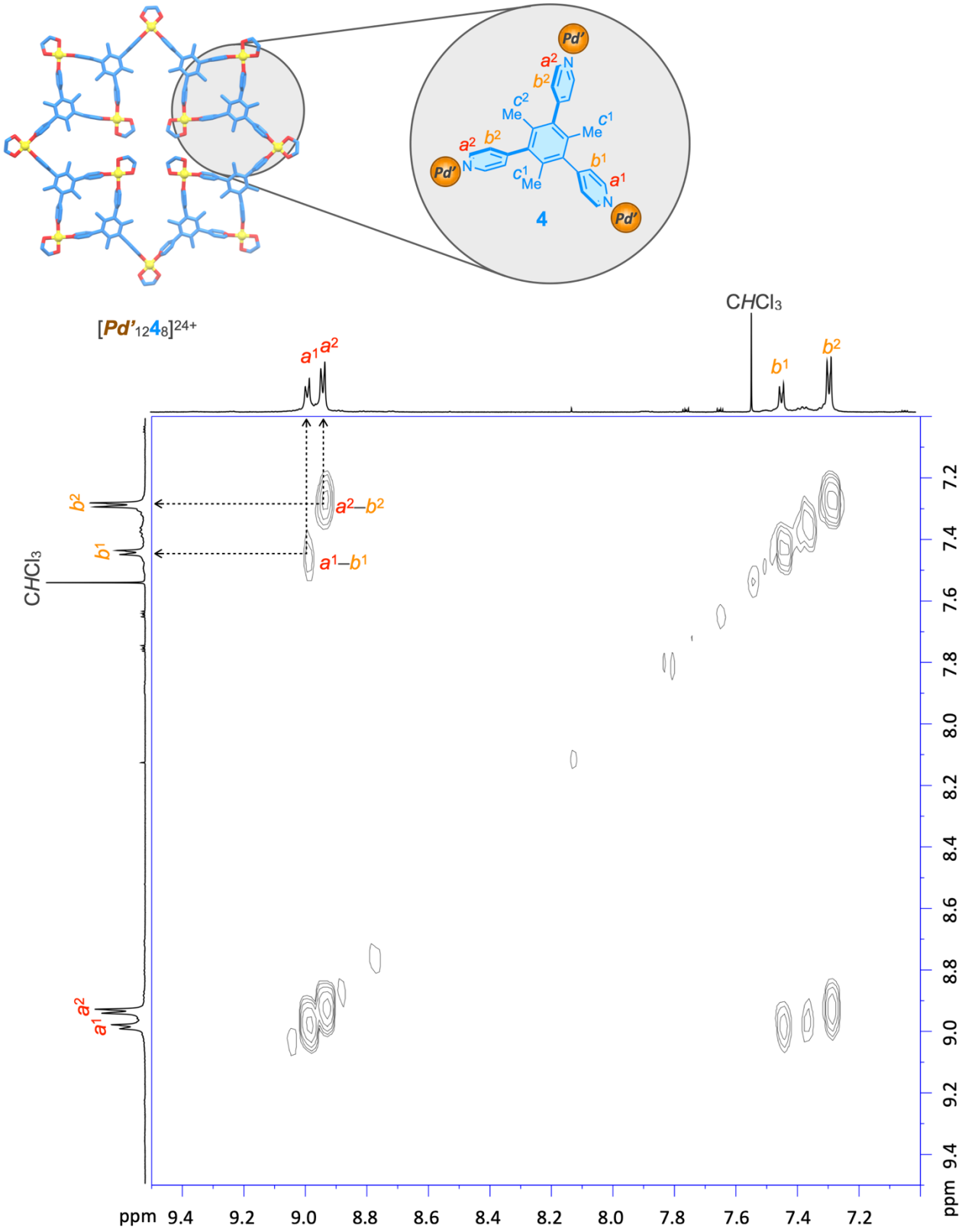

Supplementary Fig. 27. (H,H)-COSY spectrum of the [***Pd'***$_{12}$**4**$_8$]$^{24+}$ square sheet (500 MHz, CD_3NO_2, 298 K).

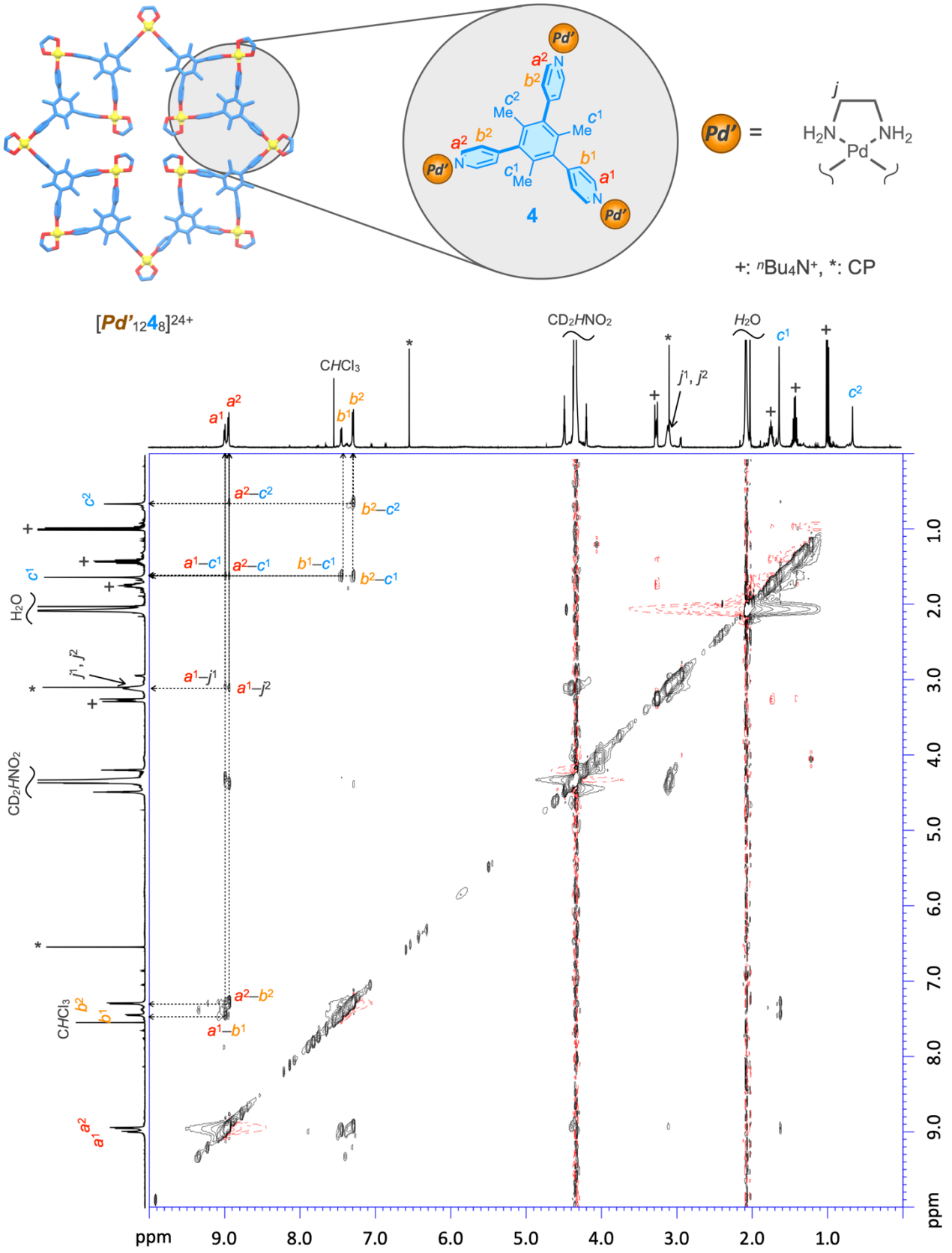

Supplementary Fig. 28. (H,H)-NOESY spectrum of the $[\boldsymbol{Pd'}_{12}\mathbf{4}_8]^{24+}$ square sheet (500 MHz, CD_3NO_2, 298 K). The signals indicated by asterisk were assigned to [2.2]paracyclophane (CP), which was included as the internal standard to determine the yield.

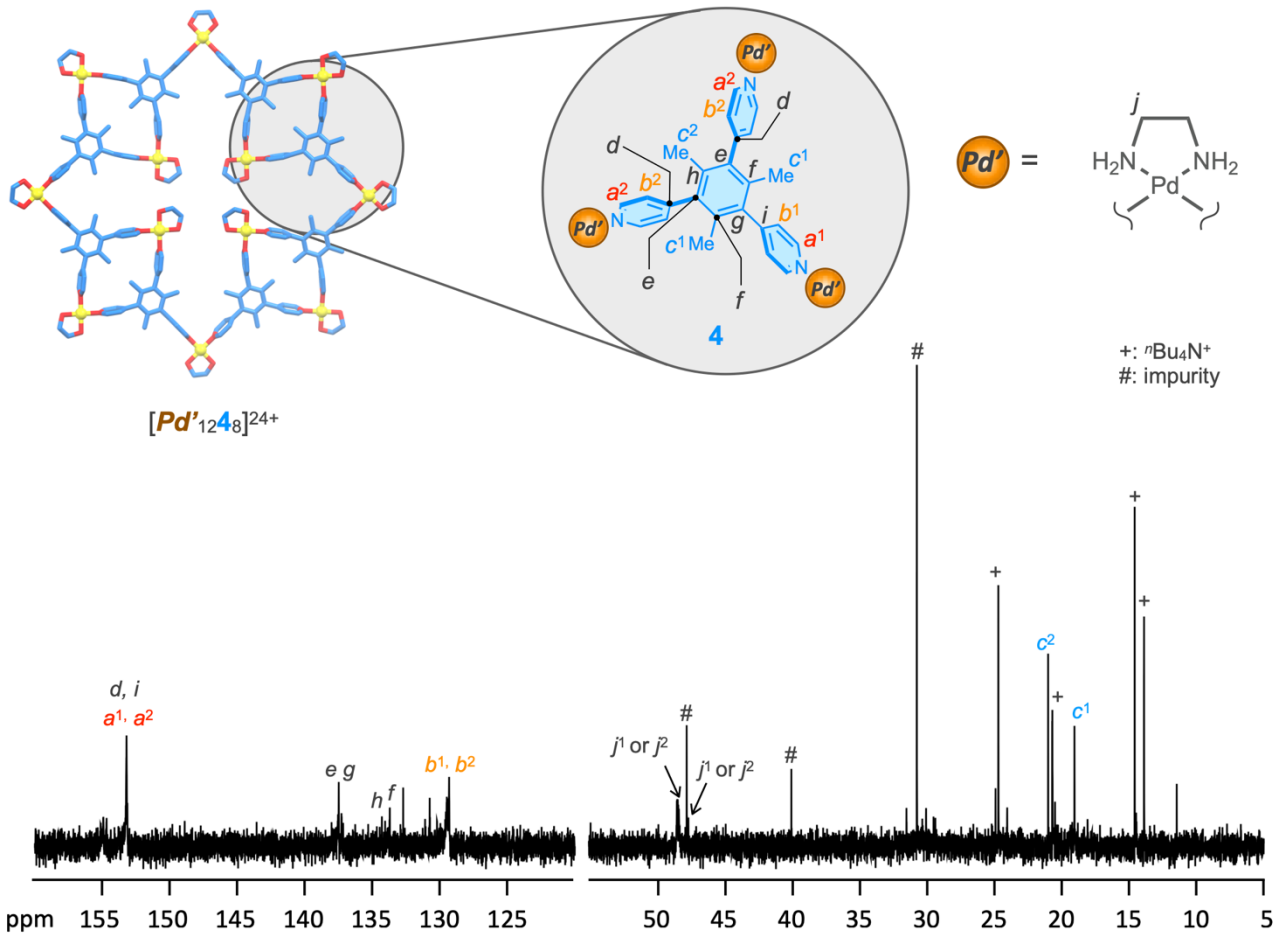

Supplementary Fig. 29. ^{13}C NMR spectrum of the $[\boldsymbol{Pd'}_{12}\boldsymbol{4}_8]^{24+}$ square sheet (500 MHz, CD_3NO_2, 298 K). The assignment of the signals was conducted based on the HSQC and HMBC spectra (Supplementary Figs. 30 and 31) and the assignment of the $[\boldsymbol{Pd'}_4\boldsymbol{4}_2]^{8+}$ ring (Supplementary Figs. 22–24).

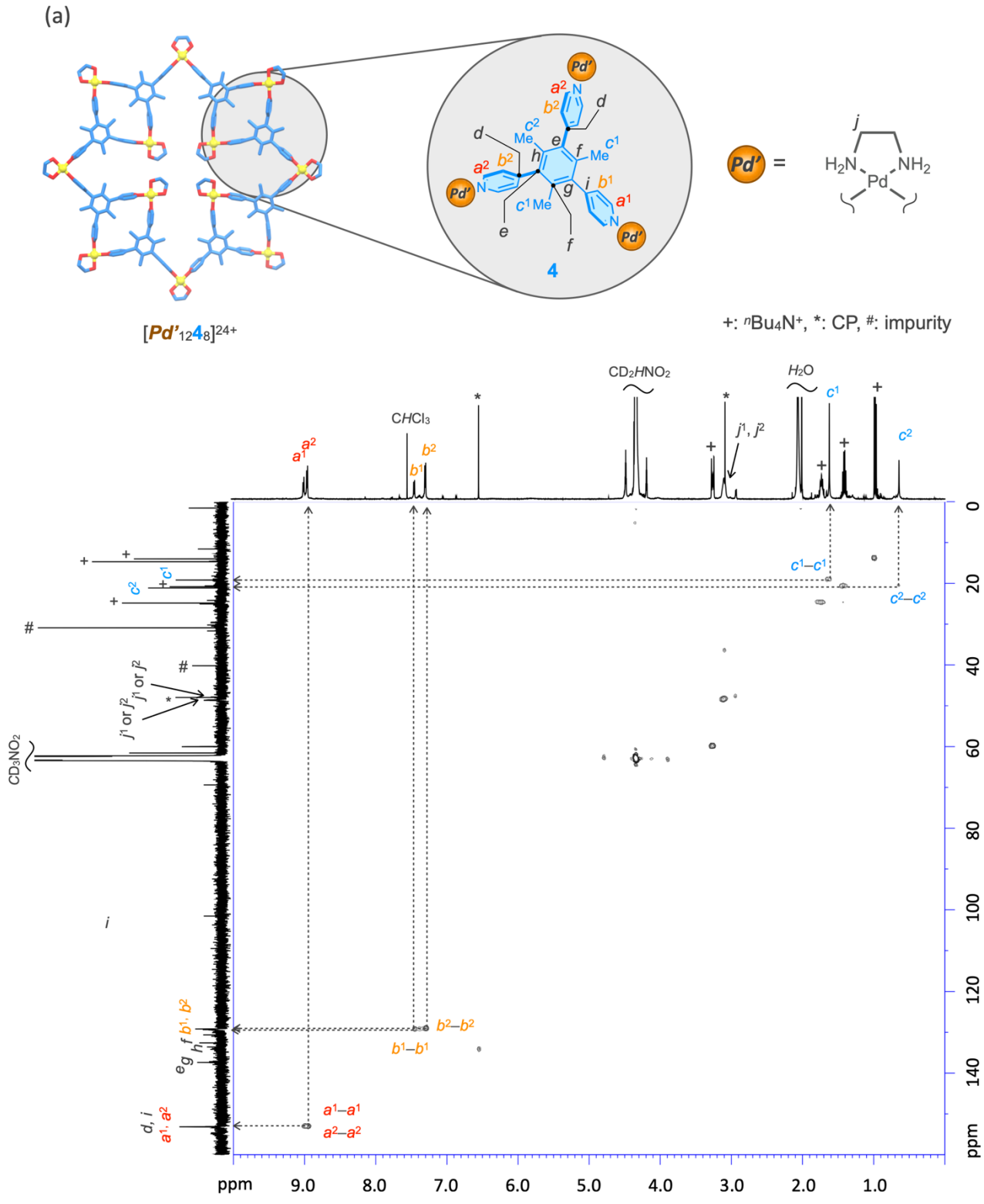

Supplementary Fig. 30. HSQC spectrum of the $[\boldsymbol{Pd'}_{12}\mathbf{4}_8]^{24+}$ square sheet (500 MHz, CD_3NO_2, 298 K). (a) overall region in the ^1H and ^{13}C spectra.

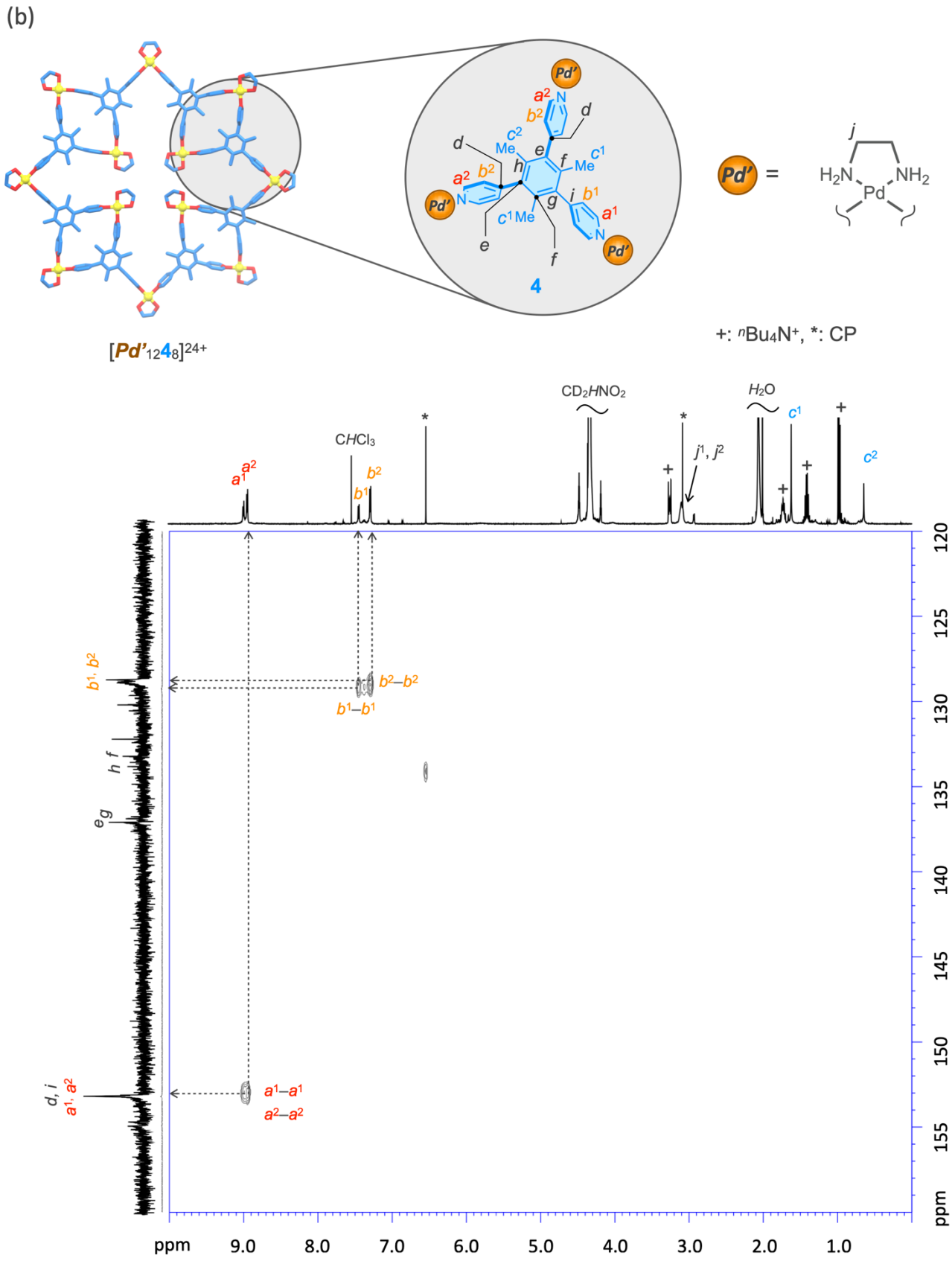

Supplementary Fig. 30. (continued) HSQC spectrum of the [***Pd'***$_{12}$**4**$_8$]$^{24+}$ square sheet (500 MHz, CD_3NO_2, 298 K). (b) overall region in the ^{1}H spectrum and aromatic region in the ^{13}C spectrum. The signals indicated by asterisk were assigned to [2.2]paracyclophane (CP), which was included as the internal standard to determine the yield.

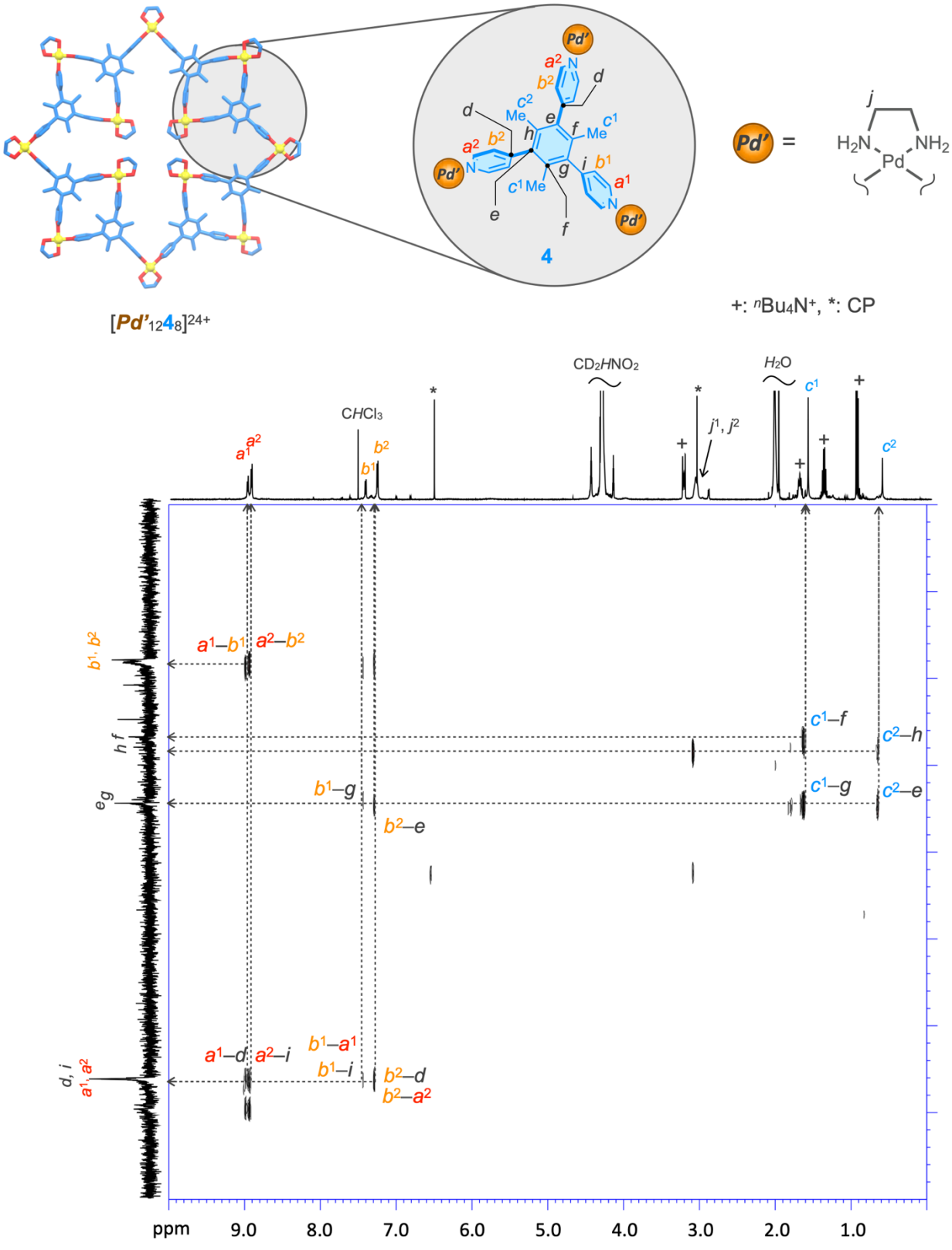

Supplementary Fig. 31. HMBC spectrum of the $[\boldsymbol{Pd'}_{12}\mathbf{4}_8]^{24+}$ square sheet (500 MHz, CD_3NO_2, 298 K). The signals indicated by asterisk were assigned to [2.2]paracyclophane (CP), which was included as the internal standard to determine the yield.

The number of isomers for the heteroleptic M_6L_4 and $M_{12}L_8$ cages

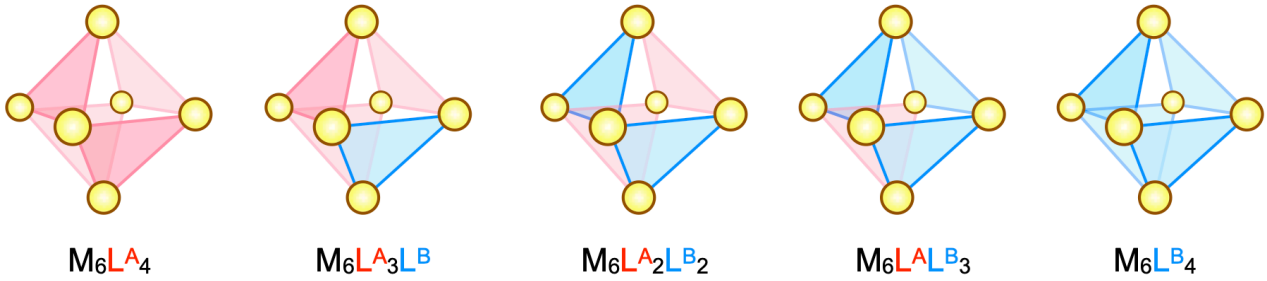

Supplementary Fig. 32. Schematic representation of isomers for the M_6L_4 open octahedron composed of two types of tritopic ligand L^A and L^B.

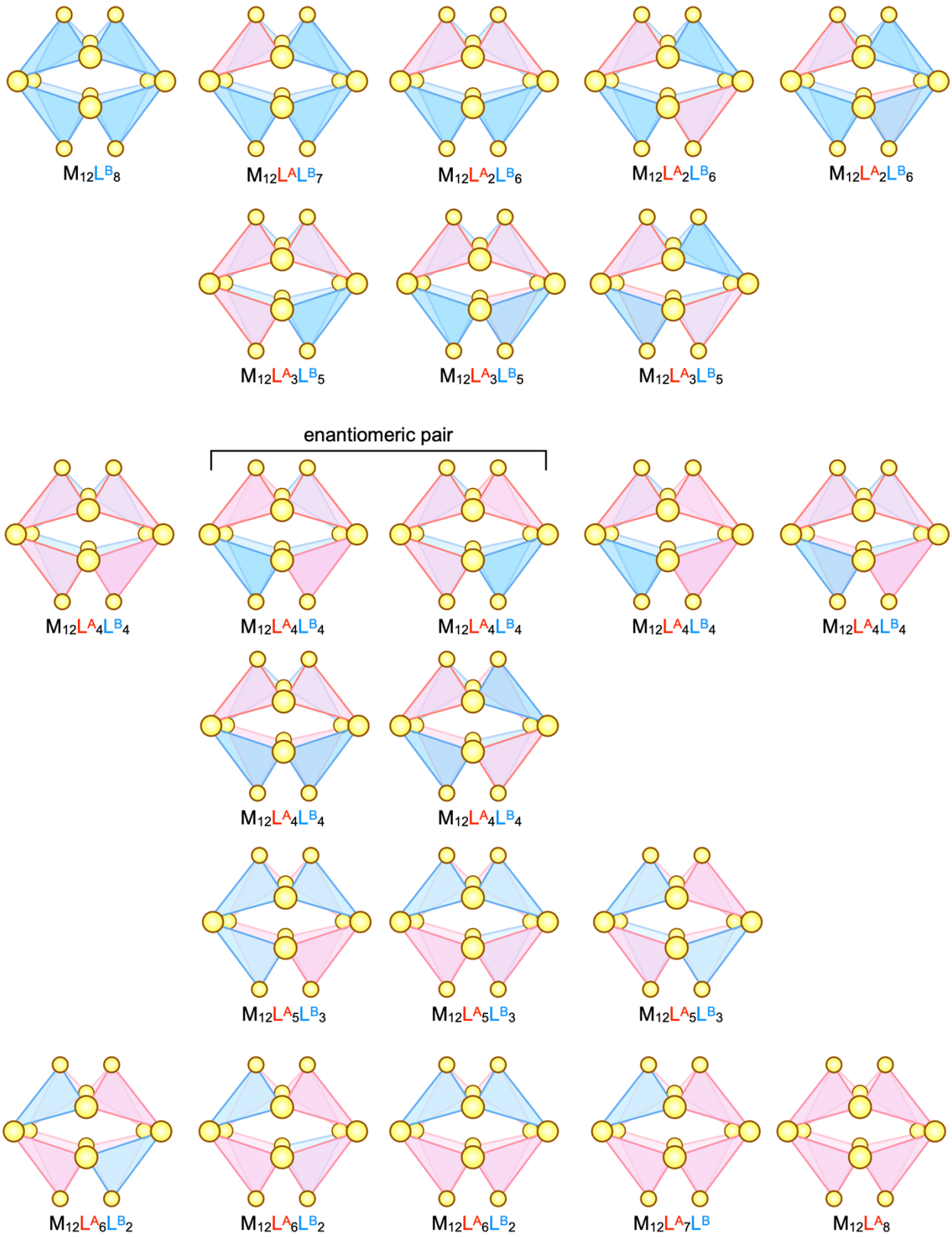

Supplementary Fig. 33. Schematic representation of isomers for the $M_{12}L_8$ open icosahedron composed of two types of tritopic ligand L^A and L^B.

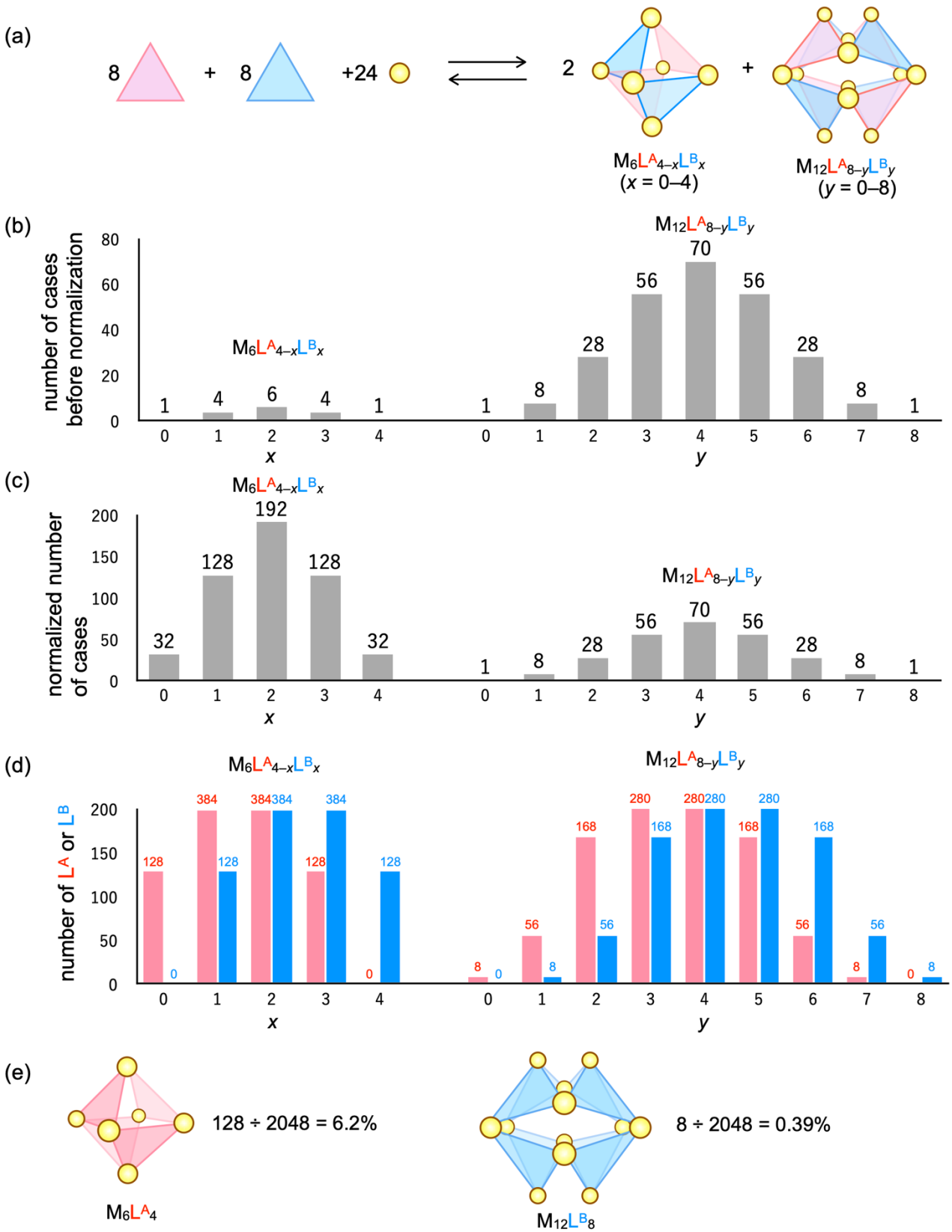

Supplementary Fig. 34. Calculations of the percentages of L^A and L^B in a statistical mixture of $M_6L^A{}_4$ and $M_{12}L^B{}_8$ in the self-assembly of L^A, L^B, and M in a 1:1:3 ratio. (a) The reaction scheme of the self-assembly considered, where it is assumed that the number of M_6L_4 is twice that of $M_{12}L_8$. (b) The number of cases for $M_6L^A{}_{4-x}L^B{}_x$ (x = 0–4) and $M_{12}L^A{}_{8-y}L^B{}_y$ (y = 0–8). (c) The number of cases for $M_6L^A{}_{4-x}L^B{}_x$ (x = 0–4) and $M_{12}L^A{}_{8-y}L^B{}_y$ (y = 0–8) after normalization by considering that the total number of cases of $M_6L^A{}_{4-x}L^B{}_x$ should be twice that of $M_{12}L^A{}_{8-y}L^B{}_y$. Therefore, because the total numbers of $M_6L^A{}_{4-x}L^B{}_x$ and $M_{12}L^A{}_{8-y}L^B{}_y$ are 16 and 256, respectively, before

normalization (in b), each number of cases of $M_6L^A_{4-x}L^B_x$ should be multiplied by 32. (d) The numbers of L^A and L^B in each $M_6L^A_{4-x}L^B_x$ and $M_{12}L^A_{8-y}L^B_y$. The total number of L^A (or L^B) in all the cases is 2048. (e) The percentages of L^A in $M_6L^A_4$ and L^B in $M_{12}L^B_8$ are calculated. In the case of the self-assembly of **1**, **2**, and ***Pd***$^{2+}$, tritopic ligands **1** and **2** correspond to L^A and L^B, respectively.

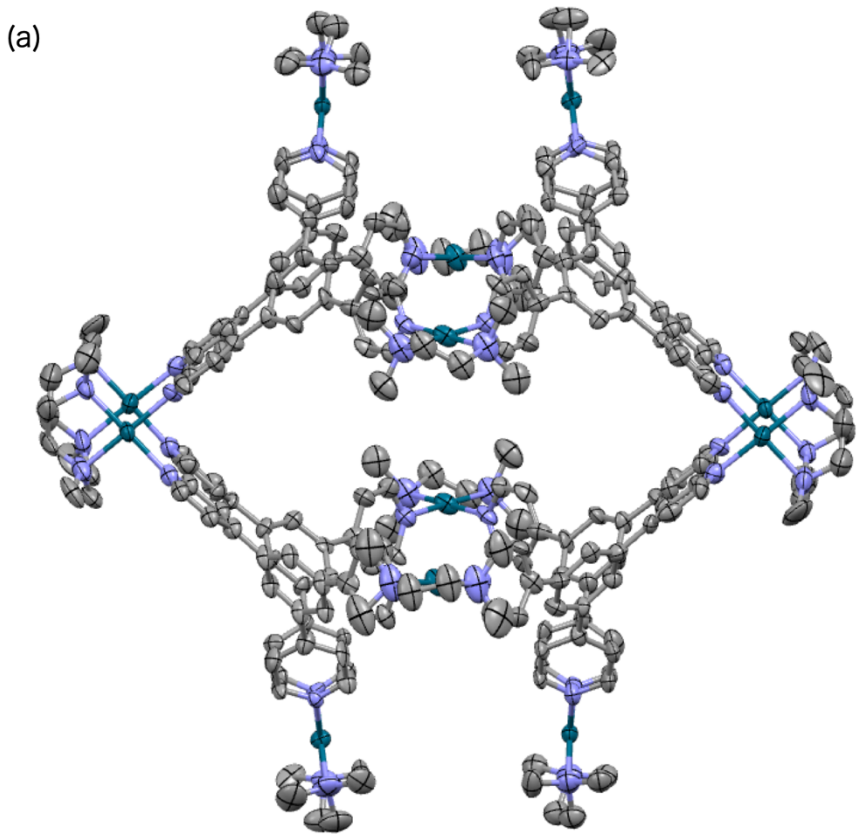

$[Pd_{12}\mathbf{2}_8]^{24+}$

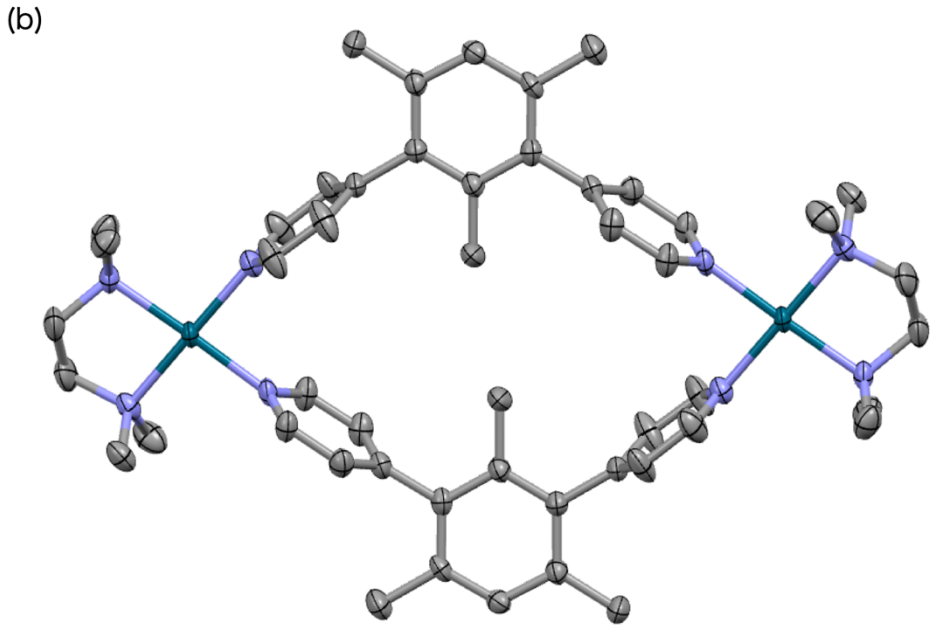

$[Pd_2\mathbf{3}_2]^{4+}$

Supplementary Fig. 35. ORTEP-drawing crystal structures of (a) $[\boldsymbol{Pd}_{12}\mathbf{1}_8]^{24+}$ (CCDC 2313022) and (b) $[\boldsymbol{Pd}_2\mathbf{3}_2]^{4+}$ (CCDC 2313023) showing 50% probability thermal ellipsoids. Color labels: Peacock green = Pd; Gray = C; Purple = N. Counter anions and hydrogen atoms are omitted for clarity.

Supplementary Tables

Energy of self-assembled structures

Supplementary Table 1. Calculated energy of [***Pd***$_6$**2**$_4$](BF$_4$)$_{12}$, [***Pd***$_9$**2**$_6$](BF$_4$)$_{18}$ and [***Pd***$_{12}$**2**$_8$](BF$_4$)$_{24}$.

Calculational methods	[***Pd***$_6$**2**$_4$](BF$_4$)$_{12}$, Hartree	[***Pd***$_9$**2**$_6$](BF$_4$)$_{18}$, Hartree	[***Pd***$_{12}$**2**$_8$](BF$_4$)$_{24}$, Hartree	Relative energy difference, kcal mol^{-1}
B3LYP/def2-SV(P)	–11833.7273481 (–5916.863674)[a]	–17750.60963 (–5916.869878)	–23667.67528 (–5916.918821)	34.6 [***Pd***$_6$**2**$_4$](BF$_4$)$_{12}$ 30.7 [***Pd***$_9$**2**$_6$](BF$_4$)$_{18}$ 0 [***Pd***$_{12}$**2**$_8$](BF$_4$)$_{24}$,
PCM(CH$_3$NO$_2$)-B3LYP/def2-SV(P) //B3LYP/def2-SV(P)	–11833.97306 (–5916.986531)	–17750.97928 (–5916.993093)	–23668.04387 (–5917.010969)	15.3 [***Pd***$_6$**2**$_4$](BF$_4$)$_{12}$ 11.2 [***Pd***$_9$**2**$_6$](BF$_4$)$_{18}$ 0 [***Pd***$_{12}$**2**$_8$](BF$_4$)$_{24}$,
PCM(CH$_3$NO$_2$)-B3LYP/def2-TZVP //B3LYP/def2-SV(P)	–11847.17434 (–5923.587168)	–17770.78041 (–5923.593469)	–23694.3967 (–5923.599174)	7.5 [***Pd***$_6$**2**$_4$](BF$_4$)$_{12}$ 3.6 [***Pd***$_9$**2**$_6$](BF$_4$)$_{18}$ 0 [***Pd***$_{12}$**2**$_8$](BF$_4$)$_{24}$,
PCM(CH$_3$NO$_2$)-B3LYP-D3(BJ)/def2-SV(P) //B3LYP/def2-SV(P)	−11835.00729 (−5917.503644)	−17752.52748 (−5917.50916)	−23670.17382 (−5917.543454)	25.0 [***Pd***$_6$**2**$_4$](BF$_4$)$_{12}$ 21.5 [***Pd***$_9$**2**$_6$](BF$_4$)$_{18}$ 0 [***Pd***$_{12}$**2**$_8$](BF$_4$)$_{24}$,
PCM(CH$_3$NO$_2$)-LC-OLYP/def2-SV(P) //B3LYP/def2-SV(P)	−11805.28825 (−5902.644126)	−17707.95331 (−5902.651104)	−23610.71569 (−5902.678923)	21.8 [***Pd***$_6$**2**$_4$](BF$_4$)$_{12}$ 17.5 [***Pd***$_9$**2**$_6$](BF$_4$)$_{18}$ 0 [***Pd***$_{12}$**2**$_8$](BF$_4$)$_{24}$,
PCM(CH$_3$NO$_2$)-M06/def2-SV(P) //B3LYP/def2-SV(P)	−11827.86567 (−5913.932835)	−17741.80832 (−5913.936108)	−23655.81935 (−5913.954836)	13.8 [***Pd***$_6$**2**$_4$](BF$_4$)$_{12}$ 11.8 [***Pd***$_9$**2**$_6$](BF$_4$)$_{18}$ 0 [***Pd***$_{12}$**2**$_8$](BF$_4$)$_{24}$,
PCM(CH$_3$NO$_2$)-ωB97X-D/def2-SV(P) //B3LYP/def2-SV(P)	−11830.88267 (−5915.441337)	−17746.34273 (−5915.447577)	−23661.92508 (−5915.481271)	25.1 [***Pd***$_6$**2**$_4$](BF$_4$)$_{12}$ 21.1 [***Pd***$_9$**2**$_6$](BF$_4$)$_{18}$ 0 [***Pd***$_{12}$**2**$_8$](BF$_4$)$_{24}$,

[a] The value in parentheses is the energy value per ***Pd***$_3$**2**$_2$(BF$_4$)$_6$ unit.

Single crystal X-ray analyses

Supplementary Table 2. X-ray crystallographic data for $[\boldsymbol{Pd}_{12}\boldsymbol{2}_8]^{24+}$ and $[\boldsymbol{Pd}_2\boldsymbol{3}_2]^{4+}$.

Compound	$[\boldsymbol{Pd}_{12}\boldsymbol{2}_8]^{24+c}$	$[\boldsymbol{Pd}_2\boldsymbol{3}_2]^{4+\,d}$
Formula	$C_{121}H_{159.5}B_6F_{24}N_{25.5}O_4Pd_6$	$C_{26.5}H_{38.5}B_2F_8N_{5.5}O_3Pd$
Formula weight	3194.49	762.15
Habit	colorless, block	colorless, columnar
Crystal size /mm	0.90 × 0.70 × 0.50	0.30 × 0.10 × 0.05
T/K	93	180
Crystal system	monoclinic	triclinic
Space group	*P*21/n	*P*-1
a/Å	29.2833(5)	8.6003(5)
b/Å	49.0051(10)	12.5383(7)
c/Å	38.5022(5)	17.0246(6)
α/°	90	96.130(4)
β/°	92.5140(10)	91.314(4)
γ/°	90	106.327(5)
V/Å^3	55198.7(16)	1749.01(16)
Z	8	2
d_{calc}/g cm^{-3}	0.769	1.447
F(000)	12944.0	776.0
μ/mm^{-1}	0.428	4.979
GOF	1.134	1.008
No. of reflns	571304	14436
Unique data	126046	14436
R_{int}	0.1426	0.0574
$R_1{}^a$ ($F^2 > 2\sigma(F^2)$)	0.1504	0.0723
$wR_2{}^b$ (all data)	0.4463	0.1974

[a] $R_1 = \Sigma||F_o| - ||F_c||/\Sigma|F_o|$.

[b] $wR_2 = [\Sigma w(F_o^2 - F_c^2)^2/\Sigma w(F_o^2)^2]^{1/2}$.

[c] The crystal structure contains a checkCIF alert (Alert B). PLAT084_ALERT_3_B. PROBLEM: High wR_2 value. RESPONSE: This alert originated from severely disordered solvent molecules in the large solvent area. The molecules are weakly trapped in the crystal, causing the large thermal ellipsolids. Therefore, the refinement had extensively used restraines in a macromolecular fashion to stabilize them. The geometry ensures a chemically and physically meaning structural model.

[d] Considering charge balance of the crystal and size of ADPs, occupancy of two BF_4^- anions were fixed to 0.5. Around these BF_4^- anions, some residual electron density peaks less than 1.0 eÅ^{-3} were found, which is presumably derived from disordered solvent molecules. However, these peaks could not be assigned to a reasonable molecular model due to the severe disorder of the solvent.